Digital Signal Processing Methods for Source Function Extraction of Piezoelectric Elements

A Thesis
Presented to
The Academic Faculty

by

Tobias Kreuzinger

In Partial Fulfillment
of the Requirements for the Degree
Master of Science in
Engineering Science and Mechanics

School of Civil and Environmental Engineering
Georgia Institute of Technology
August 2004

Digital Signal Processing Methods for Source Function Extraction of Piezoelectric Elements

Approved:

Dr. Laurence J. Jacobs, Chairman

Dr. Jennifer E. Michaels

Dr. Reginald DesRoches

Date Approved: August 18, 2004

To Mother Earth, for all her bees.

Acknowledgements

First of all, I would like to express my gratitude to Dr. Stefan Hurlebaus who gave me great support in performing all the measurements and getting an introduction to the theory of wave propagation. His background and practical experience helped me enormously to start out with my thesis at a very high level! Special thanks go to Prof. Jennifer E. Michales and Prof. Thomas E. Michaels who greatly supported me with their extensive amount of knowledge and experience. Especially Prof. Jennifer E. Michales helped me with an enormous intense of time to come along with the signal processing parts of my thesis. Furthermore she helped me finding new ideas and concepts to tackle all the problems during my research work.

Also, I am deeply indepted to my advisor Prof. Laurence J. Jacobs who knew best how to motivate me in desperate situations. Many fruitful discussions with him helped me to keep track of the big picture. I do not only want to thank him for being a great advisor but also a friend with an extraordinary ambition to help as much as possible. I thank him for his great organizational and financial commitment to give me a chance to present the results of this thesis at the 31st Annual Review of Progress in Quantitative Nondestructive Evaluation (QNDE) at the Colorado School of Mines in Golden, Colorado.

Moreover, I would like to express special thanks to Prof. Lothar Gaul for choosing me as a candidate for the ISAP Program which is financially supported by the DAAD (German Academic Exchange Service). The DAAD is gratefully acknowledged for supporting me with its scholarship.

Enabling me to finish my studies and stay abroad for 13 month, I would like to express my deepest gratitude to my family, especially to my mother, and all my friends. Furthermore I would like to thank Annette Reimet for her endless love and patience and my great friend Juergen Fritz who made not only my studies in Stuttgart an unforgettable chapter of my life. I would like to thank Kritsakorn Luangvilai for

his help during my studies and the research part of my thesis. Last but not least, I would like to thank Oliver Kotte, Hilde Maess, Andy Di Song, and all the other people in the lab for being new friends to share great memories and for supporting me during my studies at the Georgia Tech. They all contributed to making this period of time the most beneficial in my life.

Table of Contents

List of Tables

List of Figures

List of Symbols or Abbreviations

$\|\ \ \|$	magnitude
δ_{ij}	Kronecker delta
ϵ_{ij}	strain tensor
λ, μ	Lamé constants
ν	Poisson's ratio
$\hat{\omega}$	reassigned angular frequency
$\boldsymbol{\psi}$	displacement potential
ρ	density
σ_{ji}	stress tensor
σ	standard deviation
φ	displacement potential
∇	differential operator
Z	absolute pressure
r	propagation distance from source to receiver
t	simulation time
A	amplitude
c_{g}	group velocity
c_{L}	phase velocity of a longitudinal wave
c_{T}	phase velocity of a shear wave
$\mathbf{d}$	direction of particle motion
d	distance
E_{d}	energy density
E	Young's modulus
$\mathbf{f}$	body force
f	frequency
$h(t)$	window function

i	imaginary unit
sl_{e}	energy slowness
$\mathbf{p}$	direction of wave propagation
k	wavenumber
$S_{\mathrm{stft}}(\omega, t)$	short-time Fourier transform
$\mathbf{t}$	traction
$\mathbf{u}$	displacement
$\Im$	Imaginary part
$\Re$	Real part
s	sourcefunction
x_{TR}	Panametrics transducer measurement
$\hat{x}_{\mathrm{TR}}$	estimate of Panametrics transducer measurement
x_{LSR}	Laser source measurement
$G(t)$	true impulse response of unbounded medium (either plate or half space)
SNR	signal-to-noise ratio
Err	error in least squares sense
w	weighting scalar
α	shaping factor
Υ	internal and external effects of mechanical source

Summary

Guided wave techniques have great potential for the structural health monitoring of plate-like components. Previous research has demonstrated the effectiveness of combining laser-ultrasonic techniques with time-frequency representations to experimentally develop the dispersion relationship of a plate; the high fidelity, broad bandwidth and point-like nature of laser ultrasonics are critical for the success of these results. Unfortunately, laser ultrasonic techniques are time and cost intensive, and are impractical for many in-service applications. Therefore this research develops a complementary digital signal processing methodology that uses mounted piezoelectric elements instead of optical devices. This study first characterizes the spatial and temporal effects of oil coupled and glued piezoelectric sources, and then develops a procedure to interpret and model the distortion caused by their limited bandwidth and finite size. Furthermore, it outlines any inherent difficulties for time and frequency domain considerations. The deconvolution theory for source function extraction in the time - and frequency domain under the presence of noise is provided and applied to measured data. These considerations give the background for further studies to develop a dispersion relationship of a plate with the fidelity and bandwidth similar to results possible with laser ultrasonics, but made using mounted piezoelectric sources.

CHAPTER 1

Introduction

Laser ultrasonic techniques have proven to be effective in the generation and detection of guided Lamb waves in plate-like structures. Unfortunately, laser ultrasonics is both time and cost intensive, and oftentimes impractical for in-service structural health monitoring. The advantages of the laser generation of guided Lamb waves are its: point-like nature, non-contact nature (no mechanical influence on the specimen surface) and broad frequency bandwidth (in the range of 50 kHz up to 10 MHz). These attributes of laser generation allow for the measurement of well separated dispersion curves, which in turn provides the potential for quantitative structural health monitoring.

Piezoelectric sources are a cheaper and more robust alternative to a laser source, but they are not as effective in developing the dispersion relationship of a plate — the dispersion curves tend to be distorted, and it is difficult to extract single modes, making it difficult to draw conclusions about the structural health of a specimen.

This research develops a methodology to characterize the effects of a piezoelectric source, then develops techniques to compensate for any negative influence, and finally attempts to match the performance of a laser source. To understand the influence of the physics and the geometry of such a source, a forward modeling approach is presented, e.g., the temporal and spatial effects are modeled and discussed. This investigation also reveals the effects of different ways of coupling piezoelectric sources to a plate specimen. However, the main interest of this work is to inspect different inversion techniques to capture the properties of a piezoelectric source in a function — this function will be referred to a source function. A deconvolution problem is solved

to obtain such a source function, and this deconvolution is performed in the time domain with the Toeplitz recursion, and in the frequency domain with simple division. Since experimentally measured signals (which are subject of all the observations in this research) contain noise and since the deconvolution is an integral operation (which sums noise), the effects of different noise levels and each of the methods will be observed and compared.

Chapter 2 gives a general overview of the theory of wave propagation and the observed wave phenomena. It describes the theoretical origin of Lamb waves and Rayleigh waves and gives an idea of their basic features. Chapter 3 presents detailed information about the experimental setup, the involved components and the obtained data sets. As mentioned before, the main interest is to observe the dispersion relationship of plate-like structures (Lamb waves), however, since the nature of dispersive Lamb waves is very complicated, less complex waveforms are acquired for comparison reasons and to understand basic properties of the developed algorithms. Therefore, additionally to plate measurements a set of Rayleigh waves (measured on an aluminum half space) is provided. Further, in Chapter 4 the inversion theory for solving deconvolution problems in the presence of noise is presented. To provide some confidence and to confirm the results obtained from the deconvolution problems, synthetic examples are performed and discussed. The extraction of dispersion curves is explained and a method, called Reassignment, is briefly introduced. To model piezoelectric sources, a set of laser source signals is used and to find an in least squares sense ideal spatial weight distribution, an algorithm (called double iterative least squares deconvolution) is developed, tested and described. Chapter 5 discusses the results obtained from experimentally measured data. It first depicts the dispersion relationships obtained from modeling the mechanical source (forward modeling) with a set of laser source signals for spatially distributed weights and then lines out the source inversion applied to the measured signals. Therefore it first considers a single laser source signal as well as averaged laser source signals to extract source functions in the time domain. This is done for both, the plate and the half space. After that, it applies the frequency domain theory for source function extraction to the measured data

and presents the computationally obtained results. Chapter 6 analysis the results of Chapter 5. It provides some deeper insight to the source function approach itself and the effects of modeling the mechanical source by averaging and weighting single laser signals. Furthermore, the modification of reflections due to specimen boundaries and its effect on the developed methods is studied and outlined.

Note, that while this research only examines piezoelectric elements and commercial transducers, the analysis procedure is general enough to be used to interpret any mechanical source exhibiting spatial and temporal influences.

Previous researchers have used Lamb waves for material characterization (see Chimenti [7] for details), but a Lamb wave's multi-mode and dispersive nature makes interpretation of time-domain signals difficult. Other researchers (see Pinto et al. [26]) used Lamb waves in conjunction with piezoelectric elements for structural health monitoring. Note that time-frequency representations (TFR) operate on time-domain signals, are capable of resolving a plate's individual modes. TFRs are well-known in the signal processing community (see Cohen [9] for a review of TFRs). Previous research has shown that TFRs based on the short-time Fourier transform (STFT) — spectrogram, reassigned spectrogram [22]) — and the (pseudo) Wigner-Ville distribution [27] are particularly well suited for representing Lamb waves. These particular TFRs are effective in this application because of their constant time-frequency resolution over all times and frequencies [22]. Since this research deals with the extraction of source function, the deconvolution theory will be provided (for further information see Michaels [18]). Further, Michaels et al. [21] present applications of deconvolution to acoustic emission signal analysis.

CHAPTER 2

Fundamental Theory

This chapter provides a brief introduction to wave propagation in elastic solids and to the signal processing method used in this study. There are a number of authoritative and comprehensive books on wave propagation theory, for example [1] [13]. Digital signal processing is covered by [17] [9] [23].

2.1 Wave Propagation

2.1.1 Linear Elasticity and Equation of Motion

In linear elasticity, the traction t_i on a plane $n_i x_i = d$ is given by

$$t_i = \sigma_{ji} n_j, \tag{2.1}$$

where σ_{ji} is the stress tensor.

The balance of linear momentum for a body with volume V and surface S can be expressed as

$$\int_S \sigma_{kl} n_k \mathrm{d}S + \int_V \rho f_l \mathrm{d}V = \int_V \rho \ddot{u}_l \mathrm{d}V, \tag{2.2}$$

with ρ representing the material mass density and f_i the body force. Gauss' theorem applied to Equation (2.2) leads to

$$\int_V (\sigma_{kl,k} + \rho f_l - \rho \ddot{u}_l) \mathrm{d}V = 0. \tag{2.3}$$

Equation (2.3) has to be fulfilled for any arbitrary volume V of the body, and therefore the stress equations of motion becomes

$$\sigma_{kl,k} + \rho f_l = \rho \ddot{u}_l. \tag{2.4}$$

It is often more efficient to have the equations of motion given solely in terms of the displacement, u_i (as opposed to Equation (2.4), which has terms of stress σ_{ij} and displacement u_i). This can be achieved by applying Hooke's law for a homogeneous, isotropic and linear elastic medium, which is given by

$$\sigma_{ij} = \lambda \epsilon_{kk} \delta_{ij} + 2\mu \epsilon_{ij}, \tag{2.5}$$

where ϵ_{ij} is the strain tensor, related to the displacement u_i by

$$\epsilon_{ij} = \frac{1}{2}(u_{i,j} + u_{j,i}), \tag{2.6}$$

and μ and λ are the Lamé constants. Plugging Equation (2.6) into Equation (2.5) and subsequently into Equation (2.4) leads to Navier's equations of motion

$$\mu u_{i,jj} + (\lambda + \mu) u_{j,ji} = \rho \ddot{u}_i \tag{2.7}$$

$$\mu \nabla^2 \mathbf{u} + (\lambda + \mu) \nabla \nabla \cdot \mathbf{u} = \rho \ddot{\mathbf{u}}. \tag{2.8}$$

Note that in this development, body forces $\mathbf{f}$ are neglected. Solving Equation (2.8), however, is difficult, because it is a coupled partial differential equation (PDE). The Helmholtz decomposition

$$\mathbf{u} = \nabla \varphi + \nabla \times \boldsymbol{\psi}, \tag{2.9}$$

provides a convenient way to uncouple these equations. Equation (2.9) represents the three components of displacement u with the four functions φ, ψ_1, ψ_2 and ψ_3. To guarantee the uniqueness of the solution, an additional constraint

$$\nabla \cdot \boldsymbol{\psi} = 0 \tag{2.10}$$

is introduced. Substitution of Equation (2.9) (Helmholtz decomposition) into the displacement equations of motion (Equation (2.8)) leads to two uncoupled wave equations expressed in terms of the displacement potentials φ and $\boldsymbol{\psi}$

$$\nabla^2 \varphi = \frac{1}{c_{\mathrm{L}}^2} \ddot{\varphi}, \qquad \nabla^2 \boldsymbol{\psi} = \frac{1}{c_{\mathrm{T}}^2} \ddot{\boldsymbol{\psi}}, \tag{2.11}$$

whereas c_{L} represents the wave speed of the longitudinal wave (will be shown later) and c_{T} the wave speed of the vertically and horizontally polarized (transverse) shear waves,

$$c_{\mathrm{L}}^2 = \frac{\lambda + 2\mu}{\rho}, \qquad c_{\mathrm{T}}^2 = \frac{\mu}{\rho}. \tag{2.12}$$

It always holds $c_{\mathrm{L}} > c_{\mathrm{T}}$. Both wave speed equations are expressed in terms of material properties density ρ and the Lamé constants μ and λ. A relationship to material properties Young's modulus E and Poisson's ratio ν is given by

$$\lambda = \frac{E\nu}{(1+\nu)(1-2\nu)}, \tag{2.13}$$

$$\mu = \frac{E}{2(1+\nu)}. \tag{2.14}$$

The plates used for the experiments in this study are made of aluminum. Table 2.1 presents the material properties and wave speeds of aluminum.

Table 2.1: Wavespeeds and material properties of aluminum

material	$\rho[\frac{kg}{m^3}]$	c_{L} $[\frac{m}{s}]$	c_{T} $[\frac{m}{s}]$	$E[GPA]$	ν	$\lambda[GPa]$
aluminum	2700	6450	3100	70	0.35	60.5

2.1.2 Wave Phenomena

Wave phenomena discussed in this section are based on the plane wave assumption, i.e. assuming a wave with constant properties (ϵ, σ, u) on a plane perpendicular to its direction of propagation $\mathbf{p}$. Equation (2.15) shows the mathematical representation of a plane wave,

$$\mathbf{u} = f(\mathbf{x} \cdot \mathbf{p} - ct)\mathbf{d}, \tag{2.15}$$

where $\mathbf{d}$ is the unit vector defining the direction of particle motion, and c is either the longitudinal wave speed c_{L} or the transverse wave speed c_{T}. By substituting Equation (2.15) into Equation (2.8), one obtains

$$(\mu - \rho c^2)\mathbf{d} + (\lambda + \mu)(\mathbf{p} \cdot \mathbf{d})\mathbf{p} = 0. \tag{2.16}$$

Since $\mathbf{p}$ are two different unit vectors, it can immediately be seen that the two possible solutions that form the basis of wave propagation are either $\mathbf{d} = \pm\mathbf{p}$ or $\mathbf{p} \cdot \mathbf{d} = 0$:

- $\mathbf{d} = \pm\mathbf{p}$ leads to $\mathbf{p} \cdot \mathbf{d} = \pm 1$ and yields with Equation (2.16), $c = c_{\mathrm{L}}$ (see Equation (2.12)). Since $\mathbf{d}$ and $\mathbf{p}$ are linearly dependent, this represents a particle movement in the direction of propagation — a longitudinal or P-wave.

- $\mathbf{p} \cdot \mathbf{d} = 0$ yields with Equation (2.16), $c = c_{\mathrm{T}}$ (see Equation (2.12)). Now the direction of motion is normal to the direction of propagation, and the wave is called a transverse wave. If a two-dimensional plane of propagation is considered (for example, the (x_1, x_2) plane), a wave with an in-plane displacement (in the (x_1, x_2) plane) is called an SV-wave (vertically polarized), while a wave with out-of-plane displacement (in the x_3 direction) is called an SH-wave (horizontally polarized).

In a homogeneous, isotropic material, transverse and longitudinal wave speeds are independent of frequency — they are nondispersive.

2.1.2.1 Reflections of P and SV-waves

The wave types derived so far propagate independently in an infinite media. As soon as a finite media in the direction of propagation is considered, reflections and coupling will occur. An incident P-wave (SV-wave), which is reflected at a stress free boundary ($\sigma_{22} = 0$ and $\sigma_{21} = 0$) normally consists of both, a P-wave (SV-wave) and a SV-wave (P-wave). Figure 2.1 shows the reflections of an incident P and SV-wave.

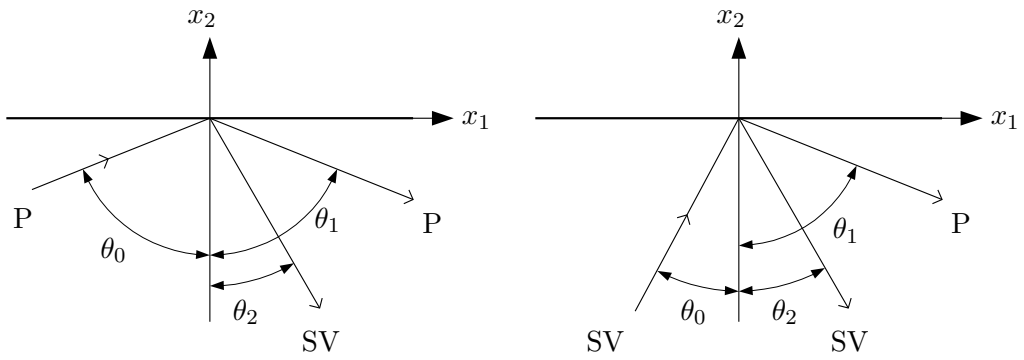

(a) Reflection of a P-wave.

(b) Reflection of a SV-wave.

Figure 2.1: Wave reflections.

The effect of a single incident wave-type producing two different waves (after reflection from a boundary) is called mode conversion. The displacement field of a harmonic wave in the x_1, x_2 plane (propagating in infinite media, plane-strain case) can be

expressed as,

$$\mathbf{u}^{(n)} = A_n \mathbf{d}^{(n)} e^{ik_n(x_1 p_1^{(n)} + x_2 p_2^{(n)} - c_n t)}, \tag{2.17}$$

whereas n denotes the wave (longitudinal or transverse), $k_n = \frac{\omega}{c_n}$ is called the wavenumber of wave n and the respective wave speeds are c_n. Using these definitions, and noting that the angular frequency ω is equal for the incident and reflected waves, it is possible to determine the relationship between the angle of the incident and the angles of the reflected waves (see Table 2.2).

Table 2.2: Angle relations for reflection on a stressfree surface

incident θ_0	reflected P θ_1	reflected SV θ_2
P	$\theta_1 = \theta_0$	$\sin\theta_2 = (c_\mathrm{T}/c_\mathrm{L})\sin\theta_0$
SV	$\sin\theta_1 = (c_\mathrm{L}/c_\mathrm{T})\sin\theta_0$	$\theta_2 = \theta_0$

Exceptions of mode conversion are the normal incidence with $\theta_0 = 0$ — in this case, the waves are reflected as themselves, and if the angle θ_0 is greater than a critical angle,

$$\theta_\mathrm{cr} = \arcsin\frac{c_\mathrm{T}}{c_\mathrm{L}}; \tag{2.18}$$

then only a SV-wave is reflected. The P-wave portion of the reflected signal degenerates into a surface wave (Rayleigh wave), traveling along the surface and exponentially decreasing in amplitude with increasing depth.

2.1.2.2 Rayleigh Surface Waves

In this research, we consider Rayleigh surface waves excited in an aluminum half space. This kind of wave has an elliptical particle motion which is retrograde with respect to the direction of propagation. One special feature of the Rayleigh wave is that it has no dispersion (that is, same velocities for different frequencies). This is an advantage in the sense of describing external effects on the waves, since we can predict the shape of the wave for different propagation distances.

To gain a better insight in the Rayleigh wave motion and its change of shape for several source receiver distances, a theoretical solution is implemented. The derivation of

this solution is outlined by Pekeris et al [25] and greatly summarized and annotated by Graff [13].

The derivation is presented for the general case where the source is buried in the material at a certain hight z, whereas for our purposes $z = 0$ which corresponds to an excitation on the surface of the half space. Furthermore the following solution is valid for the case of a step normal loading in the center of the half space. Since it is helpful for later discussions we can easily obtain the response of an impulse loading by just subtracting two step responses from each other. Then the impulse length corresponds to a time difference of the two steps. The final result for the out of plane displacement field is

$$u_z(r,z,t) = u_z(r,0,t) = \begin{cases} 0, & \tau < \frac{1}{\sqrt{3}} \\ \frac{3Z}{32\pi\mu r}\{6 - \{\frac{3}{\tau^2-\frac{1}{4}})^{\frac{1}{2}} - (\frac{3\sqrt{3}+5}{\frac{3}{4}+\frac{\sqrt{3}}{4}-\tau^2})^{\frac{1}{2}} + (\frac{3\sqrt{3}-5}{\tau^2+\frac{\sqrt{3}}{4}-\frac{3}{4}})^{\frac{1}{2}}\}, & \frac{1}{\sqrt{3}} < \tau < 1 \\ \frac{3Z}{16\pi\mu r}\{6 - (\frac{3\sqrt{3}+5}{\frac{3}{4}+\frac{\sqrt{3}}{4}-\tau^2})^{\frac{1}{2}}\}, & 1 < \tau < \gamma \\ \frac{3Z}{8\pi\mu r}, & \tau > \gamma, \end{cases} \tag{2.19}$$

where $\gamma = \frac{1}{2}(3+\sqrt{3})^{\frac{1}{2}}$.

Using

$$c_{\mathrm{T}} = (\frac{\mu}{\rho})^{\frac{1}{2}} \tag{2.20a}$$

$$\tau = \frac{c_{\mathrm{T}} t}{r} \tag{2.20b}$$

Equations (2.19) are completely described in an explicit form. The result of an impulse load of 15 ns duration and at $r = 46$ mm propagation distance is depicted in Figure 2.2.

2.1.2.3 Guided Waves

Guided waves are waves that travel in a body (waveguide) with at least one finite and one infinite dimension. So far only single reflections have been considered, but in a wave guide multiple reflections at the surface (as shown in Figure 2.3) are possible. As a result of mode conversion at the upper and lower boundaries, many propagating waves are reflected back and forth, resulting in an interference pattern across the body thickness that guides the waves in a certain direction. To investigate wave motion in

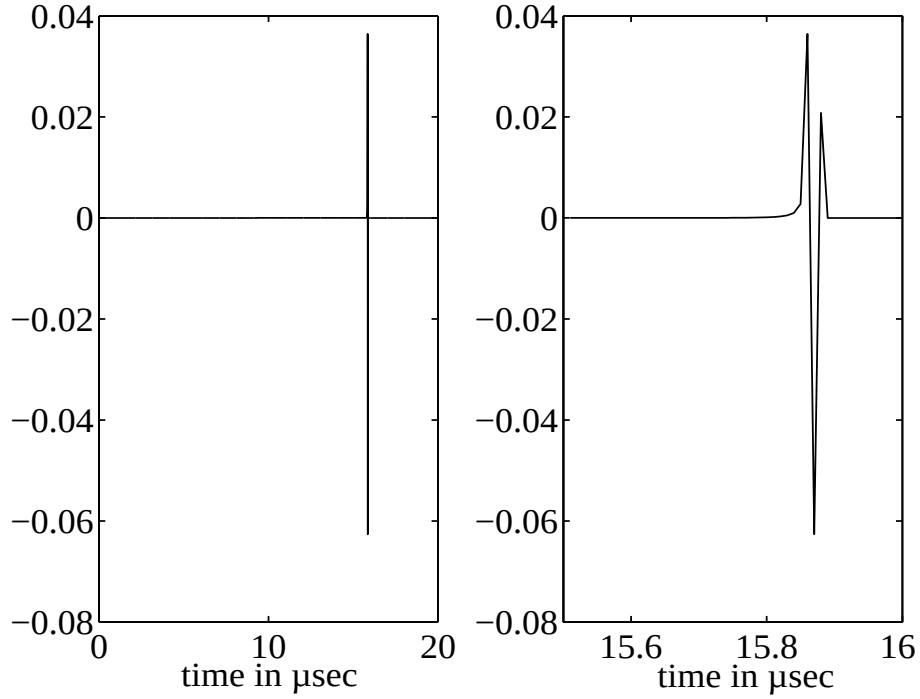

Figure 2.2: Theoretical solution for the Rayleigh surface wave.

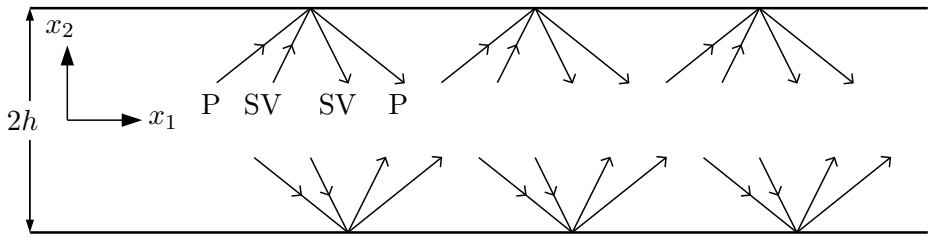

Figure 2.3: Waveguide.

an elastic wave guide, potentials in the form

$$\varphi = \Phi(x_2)e^{i(kx_1-\omega t)}, \qquad \psi_3 = \Psi(x_2)e^{i(kx_1-\omega t)}, \tag{2.21}$$

are assumed. The direction of propagation $\mathbf{p}$ is in the x_1-direction. Assuming plane strain and stress-free boundaries at $x_2 = \pm h$, one can obtain the Rayleigh-Lamb frequency equations (see Achenbach [1] for more details)

$$\frac{\tan(qh)}{\tan(ph)} = -\frac{4k^2pq}{(q^2-k^2)^2} \tag{2.22}$$

$$\frac{\tan(qh)}{\tan(ph)} = -\frac{(q^2-k^2)^2}{4k^2pq}, \tag{2.23}$$

where

$$p^2 = \frac{\omega^2}{c_{\mathrm{L}}^2} - k^2, \qquad q^2 = \frac{\omega^2}{c_{\mathrm{T}}^2} - k^2, \tag{2.24}$$

and $2h$ is the plate thickness. Equation (2.22) represents the symmetric Lamb modes, while Equation (2.23) provides the antisymmetric Lamb modes. (Anti)symmetric is understood to be that the displacement is (anti)symmetric to the x_1-axis and a Lamb mode is an amplitude distribution over the plate thickness that oscillates with the angular frequency ω and travels with the corresponding phase velocity $c = \frac{\omega}{k}$ obtained from an (ω, k) solution pair of the Rayleigh-Lamb spectrum (Equations (2.22) and (2.23)). Note that Lamb waves are dispersive, i.e., the propagation velocity of a Lamb mode is dependent on its oscillation frequency. The Rayleigh-Lamb equations can only be solved numerically and Figure 2.4 shows a solution (dispersion curves) of the Rayleigh-Lamb spectrum in the slowness-frequency domain. The symmetric Lamb modes are named $s_0, s_1, \ldots$ and the antisymmetric $a_0, a_1, \ldots$ starting with the mode that has the lowest angular frequency ω for a given k. The dispersion curves are obtained by finding first a numerical solution in the (ω, k)-domain or (f, k)-domain respectively and differentiating f numerically (partially with respect to k) for each of the different modes to attain the group velocity

$$c_g(f) = \frac{2\pi\partial f}{\partial k}. \tag{2.25}$$

Group velocity as defined in Equation (2.25) describes the velocity of propagating energy and has therefore a physical meaning. In contrast, points of constant phase

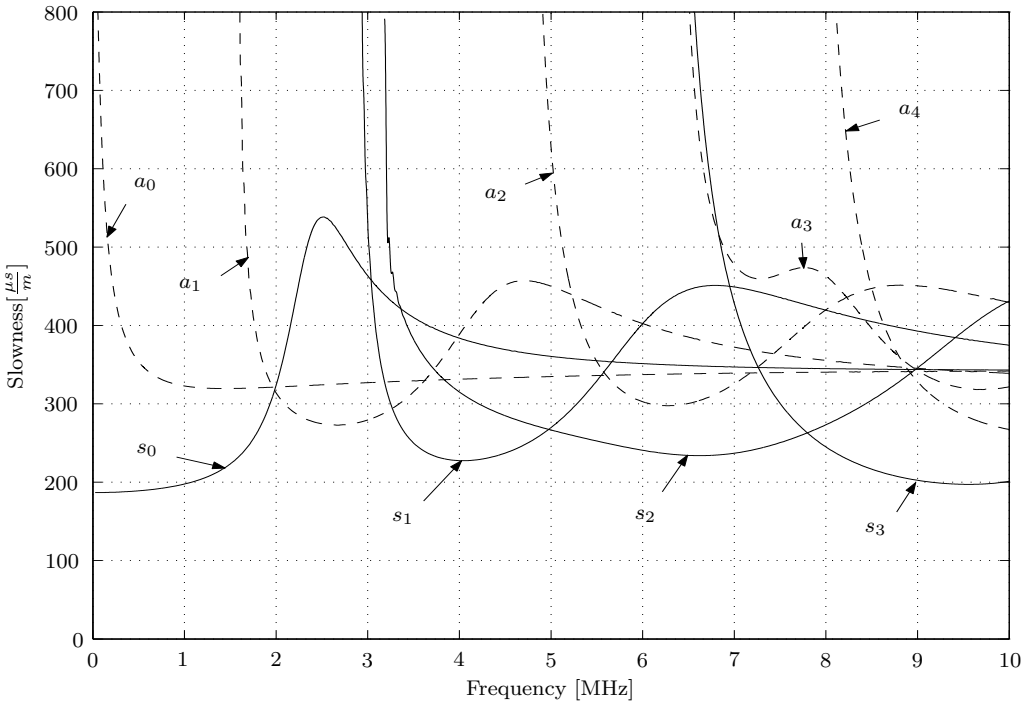

Figure 2.4: Theoretical solution in slowness-frequency domain (dispersion curves).

propagate with the phase velocity $c = \frac{\omega}{k}$. However, for nondispersive media, group and phase velocity are equal.

The energy slowness sl_e can then be obtained by the relationship

$$sl_e(f) = \frac{1}{c_g(f)}. \tag{2.26}$$

If the theoretical solution in the time-frequency domain is required, they are found by

$$t(f) = \frac{sl_e(f)}{d}; \tag{2.27}$$

the expected arrival time for a specific mode at frequency f, where d is the propagation distance source-receiver. The theoretical dispersion curves are calculated using the numerical code Disperse developed by Pavlakovic et al [24], using material properties that are measured independently with bulk ultrasonic waves.

Existing Matlab code is modified to perform a normal mode expansion and calculate theoretical Lamb waves for a plate that is 1 mm thick and considered infinite. The waveform of the theoretical Lamb waves is obtained by superimposition of the first 6 symmetric and anti-symmetric modes with a modeled sampling frequency of 100 MHz. Further information about how to implement dispersion curves, expand the normal modes and obtain formula for the theoretical Lamb wave is given by Pao [30]. Equivalent to the Rayleigh wave simulation in Section 2.1.2.2, the source receiver distance is 46 mm and the simulated impulse duration is 15 ns. Figure 2.5 depicts the results for the theoretical Lamb wave.

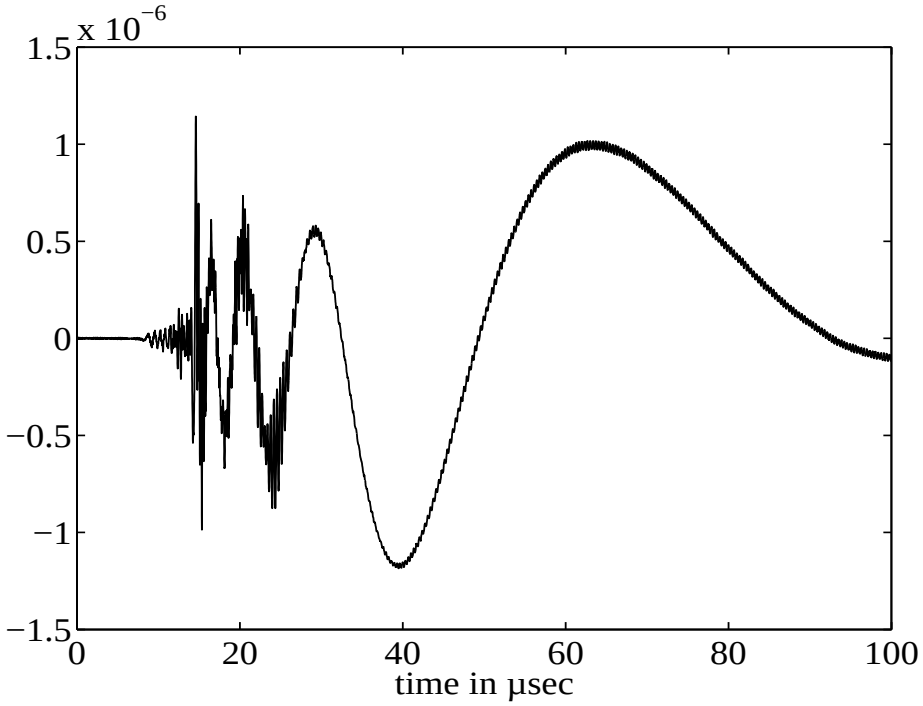

Figure 2.5: Theoretical solution for the Lamb wave.

2.2 Digital Signal Processing Background

2.2.1 Fourier Series

The Fourier series of a T-periodic function $s(t)$ is

$$S_s(t) = \sum_{k=-\infty}^{\infty} c_k e^{ik\omega t} \tag{2.28}$$

with the coefficients c_k computed by

$$c_k = \frac{1}{T} \int_0^T s(t) e^{-ik\omega t} \mathrm{d}t \tag{2.29}$$

where $\omega = \frac{2\pi}{T}$ is called the fundamental frequency.

While Equation (2.29) is used to break down the original signal $s(t)$ into its spectral components; i.e., into components of different frequencies $\omega_k = k\omega, k \in \mathbb{Z}$, Equation (2.28) combines the different spectral components into an infinite series that represents the original signal. Clearly, the resulting Fourier series $S_s(t)$ is also T-perodic and composed of sines and cosines with frequency ω and their harmonics[1]. For computer implementation, the discretized version of the Fourier series (DFS)

$$\tilde{s}[n] = \frac{1}{N} \sum_{k=0}^{N-1} \tilde{S}[k] e^{\frac{-i2\pi kn}{N}} \tag{2.30}$$

can be derived [23], where

$$\tilde{S}[k] = \sum_{n=0}^{N-1} \tilde{s}[n] e^{\frac{i2\pi kn}{N}} \tag{2.31}$$

are the coefficients of the DFS and N is the sequence length. Note that in the discrete case, it is sufficient to have at most N different frequency components to completely synthesize the original sequence $s[n]$ by the DFS Synthesis Equation (2.30); this is in contrast to an infinite number required in the continuous case.

Since the DFS is not "aware" of the sampling frequency of the sequence $s[n]$, the index k for $\tilde{S}[k]$ has to be converted from the normalized frequency $f = \frac{k}{N} \in [0, 1]$ to

[1] since $e^{it} = \cos t + i \sin t$

the real frequency f. The corresponding frequency for a given $\tilde{S}[k]$ is

$$f = \frac{k}{N} f_\mathrm{s} \tag{2.32}$$

with f_s being the sampling frequency of the sequence $s[n]$. One should keep in mind that whenever continuous signals are discretized, frequencies with $f \leq \frac{f_\mathrm{s}}{2} = f_\mathrm{N}$, where f_N is the Nyquist frequency, can only be unambiguously identified if the signal itself is limited to a frequency band below the Nyquist frequency. Otherwise aliasing can occur for higher frequencies; i.e., it is possible that a higher frequency appears as a lower frequency in the sampled domain, thus creating spurious information.

2.2.2 Fourier Transform

In contrast to the periodic Fourier series, the Fourier transform represents the limiting case of the series for $T \to \infty$. It allows for the representation of an aperiodic function $s(t)$ by the Fourier integral

$$s(t) = \frac{1}{2\pi} \int_{-\infty}^{\infty} e^{i\omega t} S(\omega) \mathrm{d}\omega, \tag{2.33}$$

where the coefficients $c(\omega)$ are defined as

$$S(\omega) = \int_{-\infty}^{\infty} e^{-i\omega t} s(t) \mathrm{d}t \tag{2.34}$$

and $S(\omega)$ is called the Fourier transform of $s(t)$. While the Fourier series represents a signal in terms of a fundamental angular frequency ω_0 and its harmonics, the Fourier transform uses a continuous angular frequency variable ω, which is related to the frequency f by

$$\omega = 2\pi f. \tag{2.35}$$

As for the Fourier series, there also exists a Fourier transform that operates on sequences. The corresponding equations are

$$s[n] = \int_{0}^{2\pi} S(\omega) e^{i\omega n} \mathrm{d}\omega \tag{2.36}$$

for synthesis and

$$S(\omega) = \frac{1}{2\pi} \sum_{n=-\infty}^{\infty} s[n] e^{-i\omega n} \tag{2.37}$$

for analysis.

The Fourier transform $S(w)$ of an input sequence $s[n]$ is thus a continuous function. It can be shown [23] that the DFS coefficients $\tilde{S}[k]$ of the sequence $\tilde{s}[n]$ are samples of the Fourier transform of $s[n]$. From this point of view, the discrete Fourier series is also called the discrete Fourier transform (DFT).

The frequency for a given $S(\omega)$ is calculated by Equation (2.35). If the signal length is a power of 2,[2] the calculation time of the DFT can be lowered significantly by the fast Fourier transform algorithm proposed by Cooley and Tukey (see for example [23]). Since the Fourier transform and the DFT are usually complex valued (where $|S(\omega)|$, $|\tilde{S}[k]|$ are the magnitudes and $atan\left(\frac{\Im(S(\omega))}{\Re(S(\omega))}\right)$, $atan\left(\frac{\Im(\tilde{S}[k])}{\Re(\tilde{S}[k])}\right)$ the phase angles for a frequency), they are frequently presented (visualized) by the energy density spectrum which represents the energy distribution in the frequency domain and is calculated by

$$E_d = |S(\omega)|^2. \tag{2.38}$$

Its discrete counterpart is

$$\tilde{E}_d[k] = \frac{1}{N} \tilde{S}[k] \overline{\tilde{S}[k]}, \tag{2.39}$$

where $\overline{\tilde{S}[k]}$ is the conjugate complex of $\tilde{S}[k]$.

2.2.3 Short-Time Fourier Transform (STFT)

The STFT

$$S_{stft}(\omega, t) = \frac{1}{2\pi} \int_{-\infty}^{\infty} e^{-i\omega\tau} s(\tau) h(\tau - t) \mathrm{d}\tau, \tag{2.40}$$

where $h(t)$ is a window function, is based on the Fourier transform. Instead of considering a transform of the entire signal at once, the signal is chopped into a series of

[2] If it is not, the signal can be zero-padded, i.e., zeros are appended at the end of the signal. This does not change the result of the transform (in the sense that the value of the transform does not change for the original discrete frequencies before and after zero-padding), but improves the frequency resolution.

small overlapping pieces, and each of these pieces is windowed and then individually Fourier transformed. Its energy density spectrum

$$E_{\mathrm{d}}(\omega, t) = |S_{\mathrm{stft}}(\omega, t)|^2 \tag{2.41}$$

is called a spectrogram.

So far it seems like the TFRs are perfect, especially when compared to the 2D Fourier transform. In theory, it appears that one measurement is enough to develop a representation that can quantify changes in a signal's frequency content as a function of time. If this is the case, there would be no point in using the 2D Fourier transform. Unfortunately, TFRs like the scalogram or the spectrogram suffer from what is known as the Heisenberg uncertainty[3], meaning (in the case of signal processing) that it is not possible to have a perfect resolution in time and frequency simultaneously.

Stating the uncertainty principle in equation form requires a set of preliminary definitions. The square norm $\|s(t)\|$ of a function $s(t)$ is defined as

$$\|s(t)\| = \left(\int_{-\infty}^{\infty} |s(t)|^2 \mathrm{d}t \right)^{\frac{1}{2}}. \tag{2.42}$$

The normalized function $s_{\mathrm{n}}(t)$ is then given by

$$s_{\mathrm{n}}(t) = \frac{s(t)}{\|s(t)\|}. \tag{2.43}$$

Since the square norm of a normalized function is equal to one, the squared magnitude is regarded as a probability density function enabling one to calculate the mean time of a function $s(t)$ by

$$E[t] = \int_{-\infty}^{\infty} t|s_{\mathrm{n}}(t)|^2 \mathrm{d}t \tag{2.44}$$

and the mean angular frequency by

$$E[\omega] = \int_{-\infty}^{\infty} \omega|S_{\mathrm{n}}(\omega)|^2 \mathrm{d}\omega, \tag{2.45}$$

[3]In fact the term uncertainty is misleading. There is no element of chance or probability as far as signal processing is concerned; instead it is a completely deterministic phenomenon.

where $S_{\mathrm{n}}(\omega)$ is the normalized Fourier transform of the function $s(t)$. The variances for t and ω are then

$$\sigma_t^2 = \int_{-\infty}^{\infty} (t - E[t])^2 |s_{\mathrm{n}}(t)|^2 \mathrm{d}t \tag{2.46}$$

and

$$\sigma_\omega^2 = \int_{-\infty}^{\infty} (\omega - E[\omega])^2 |S_{\mathrm{n}}(\omega)|^2 \mathrm{d}\omega. \tag{2.47}$$

The uncertainty principle limits the possible resolutions by the inequality

$$\sigma_t^2 \sigma_\omega^2 \geq \frac{1}{4}. \tag{2.48}$$

Therefore, the standard deviation in time and frequency cannot be varied independently, but they are related to each other.

2.2.4 Representation of Dispersion Curves

As mentioned in Section 2.2, time-frequency representations (TFR), i.e., the spectrogram, cannot simultaneously have perfect resolution in both time and frequency due to the Heisenberg uncertainty principle. Thus, the resulting representation is unsatisfactory for many applications. But it is possible to improve the time-frequency resolution of a spectrogram with an algorithm that is referred to as reassignment [2]. In the following steps, the basic idea of the reassignment method is presented.

In reassignment, values are moved away from their point of computation to their center of gravity, thus localizing the diffuse information of the time-frequency representation. The reassignment method is not restricted to a specific TFR, but it can be applied to any time-frequency shift invariant distribution of Cohen's class. This class of TFRs was a representation presented by Cohen et al [9, 2, 16] and later resolved to the easier version developed by Auger and Flandrin [2]. These researchers show that the reassigned coordinates $\hat{t}$ and $\hat{\omega}$ for the spectrogram can be calculated as

$$\hat{t} = t - \mathrm{Re}\left(\frac{STFT_{\mathcal{T}h}(x,t,\omega) \cdot \overline{STFT_h(x,t,\omega)}}{|STFT_h(x,t,\omega)|^2} \right) \tag{2.49}$$

and

$$\hat{\omega} = \omega - \mathrm{Im}\left(\frac{STFT_{\mathcal{D}h}(x,t,\omega) \cdot \overline{STFT_h(x,t,\omega)}}{|STFT_h(x,t,\omega)|^2} \right) \tag{2.50}$$

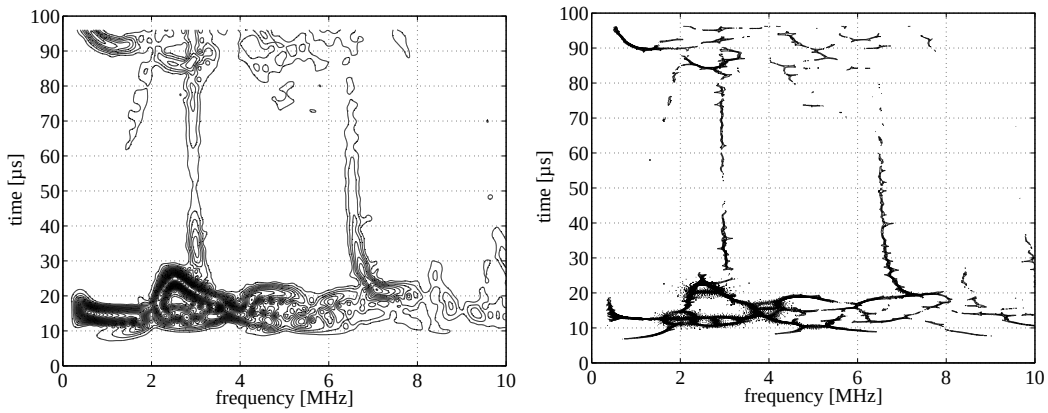

(a) Normal spectrogram of single laser. (b) Reassigned spectrogram of single laser.

Figure 2.6: Comparison between normal and reassigned spectrogram.

for the STFT, where $STFT_h(x,t,\omega)$ is the short time Fourier transform of the signal x using a normalized window function $h(t)$; $STFT_{\mathcal{T}h}(x,t,\omega)$ and $STFT_{\mathcal{D}h}(x,t,\omega)$ are the short time Fourier transforms with $t \cdot h(t)$, $\frac{\mathrm{d}h(t)}{\mathrm{d}t}$ as their respective window functions.

The reassignment algorithm relocates each time-frequency point from the coordinates (t,ω) to a new, reassigned position $(\hat{t}(t,\omega),\hat{\omega}(t,\omega))$. This relocation can be expressed by the displacement vector field

$$\mathbf{r}(t,\omega) = \begin{pmatrix} \hat{t}(t,\omega) - t \\ \hat{\omega}(t,\omega) - \omega \end{pmatrix} \tag{2.51}$$

defined by Equations (2.49) and (2.50).

If several points from the spectrogram are moved to the same point in the reassigned representation, their amplitudes are added up, thus conserving the energy. Calculating the reassignment of a spectrogram (Figure 2.6(b)) produces a much more distinct time-frequency representation when compared to a non-reassigned spectrogram (Figure 2.6(a)). From now on, all TFRs will be presented in the reassigned representation — except explicitly denoted differently.

CHAPTER 3

Experimental Procedure

This chapter describes and illustrates the experimental procedure. While Section 3.1 describes the individual system components which are used in the experiments, Section 3.2 presents the physical arrangement of these components and describes the performance of the experiments.

3.1 Experimental System

The basic components needed to perform the experiments are: a source system, a detection system, the specimen, and any additional instrumentation to analyze the data.

3.1.1 Source Systems

3.1.1.1 Laser source

The laser used as the laser source is a Q-switched, Nd:YAG laser with a power output of 405 mW (650 mJ) and a wave length of 1064 nm. The laser emits pulses only with a pulse length of 4 to 6 ns. Since the laser light at this wavelength is invisible, a He-Ne laser is used to align the source laser and the beam of this He-Ne laser is controlled to be coaxial to the Nd:YAG laser beam. Figure 3.1 shows the source system and the path of the two laser beams (Nd:YAG and He-Ne). The mirror between the absorption plate and the lens (Figure 3.1), is mounted on a translation stage. As will be described later, this translation stage is needed to perform a variety of measurements with different propagation distances.

A laser source is used in these experiments because: it excites a broad frequency

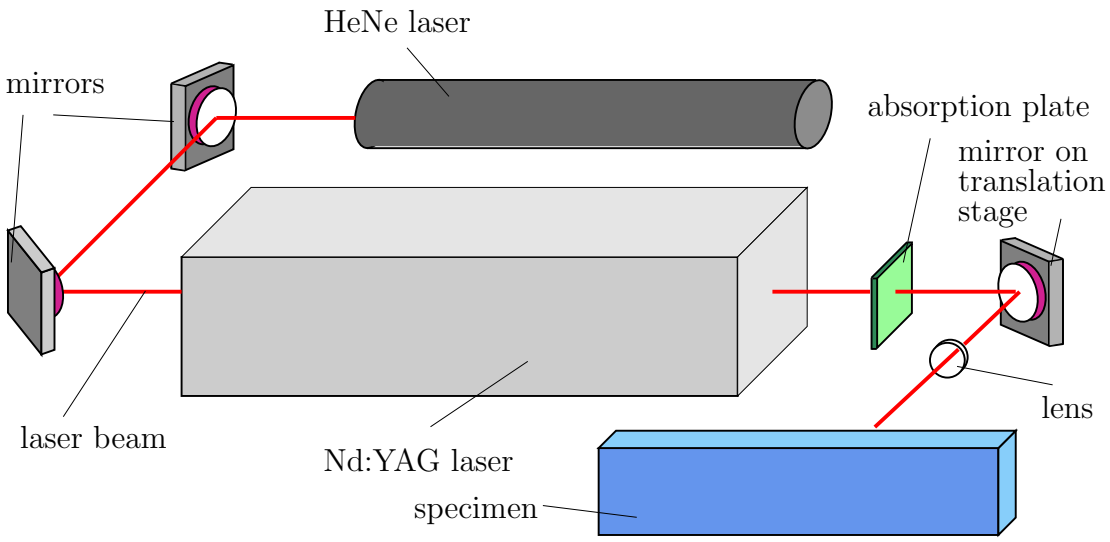

Figure 3.1: Scheme of source system.

bandwidth (typically frequencies from 100 kHz to 10 MHz are excited with this optical source); the laser source is non-contact so there are no coupling effects associated with it, leading to good repeatability of the laser source; and because it is a point source, which enables modeling of finite sources by convolution and is free of near-field transducer effects, such as diffraction effects.

Generally, there are two types of laser sources possible: ablation and thermoelastic. The difference between these two sources is the amount of laser energy (relative energy, depending on a number of factors such as source spot-size). An ablation source is created with more laser energy than a thermoelastic source. The advantage of using a thermoelastic source is that it is truly nondestructive — a thermoelastic source does not damage the specimen's surface, but the energy level of ultrasonic (acoustic) waves, excited with a thermoelastic source, is low. In contrast, an ablation laser source excites ultrasonic waves with higher energy, which leads to better signal-to-noise-ratio (SNR) — an ablation source is used in these experiments. An ablation source, however, vaporizes a thin layer of material at the excitation point — the point where the Nd:YAG laser beam hits the specimen. Eisenhardt [12] examines

the repeatability of an ablation source with an emphasis on spot size and frequency bandwidth, and determines that the ablation source is very repeatable in terms of frequency, as long as the spot size remains constant. Note that each measurement represents an average of 20 laser pulses; this signal averaging increases SNR by a factor of $\sqrt{N}$, where N is the number of averages.

The experimental procedure uses a set of absorption plates and focusing lenses to control laser energy and spot size at the laser source, and thus source type (ablation versus thermoelastic). Figure 3.1 shows the location of the absorption plate and focusing lens, and a consistent laser source is ensured following the procedure described by Eisenhardt [12]. Note that the current research uses an ablation source in all the experiments.

3.1.1.2 Piezoelectric Sources

Two different types of piezoelectric sources are used in this research. The first one is a commercial *Panametrics V544*[1] transducer that works at a center frequency of 10 MHz and has a nominal element diameter of 6 mm. Several coupling materials like commercial engine oil, soap and food oil were tested for measurements with this transducer. The piezo in the transducer is embedded in a housing that contains a backing unit to minimize reflections in the transducer. Basically, the backing absorbs all the waves propagating towards the housing. The electronic connection is realized with a screw connector that contains the negative as well as the positive pole. This source will be referred to as the "commercial transducer" source in the reminder of the thesis.

The second piezoelectric source is a LTZ-5 piezo (PZT), ceramic crystal. Its center frequency is roughly 10 MHz. Since this crystal is extremely small (0.24 mm in height and 5.2 mm in diameter) it is only coupled to a specimen with glue. This source will be referred to as the "piezo disc" source in the reminder of the thesis. The bottom part of the piezo disc is the negative pole and the top layer is the positive pole. This

[1] produced by Panametrics-NDT, Waltham, MA, USA
(*http://www.panametrics-ndt.com*)

property of the ceramic disc requires a conductive glue. A very effective glue is the *MG Chemicals*[2] silver conductive epoxy which forms high strength bonds on the one hand and is highly conductive on the other. The electronic connection is a spring construction, where 4 springs touch the plate surface and one spring touches the top of the piezo disc. The advantage of this connection over a soldered connection is that one does not have to heat up the crystal, i.e., it does not change its material structure, and the influence of the cable connection on the oscillation behavior can be neglected.

Both piezoelectric sources are driven by a *Panametrix* 35 Mhz ultrasonic pulser-receiver, model 5072PR[3].

3.1.2 Detection System

The detection system used in this study is a dual probe heterodyne interferometer that uses a 2 Watt Argon-ion-laser with a wavelength of 514.5 nm. This interferometer is a modified version of the system developed as a single probe system described in Bruttomesso et al [5] but later extended to a dual probe system by Hurlebaus [15].

The working principle of this interferometric system is the Doppler effect, which enables measurement of the absolute particle velocity of a point on the specimen's surface. Figure 3.2 (similar to [15]) shows the physical setup of the dual probe interferometer.
In brief, the Argon laser produces a single beam of vertically polarized light. A $\lambda/2$-plate rotates this beam into 45° polarized light, which is a superposition of horizontally and vertically polarized light. The polarized beam passes through an acousto-optic modulator (AOM) that splits the rotated beam into basically 2 beams. One beam, which travels to the object (specimen) and is reflected off the object (referred to as the object beam), while the other one serves as a reference (called the reference beam). An AOM is comprised of a Bragg cell, which is excited by a piezoelectric transducer,

[2]produced by MG Chemicals, Surrey, BC, Canada
($http://www.mgchemicals.com$)
[3]data sheet can be found under
($http://www.panametrics-ndt.com/nedt/pulser_receivers/downloads/5072pr.pdf$)

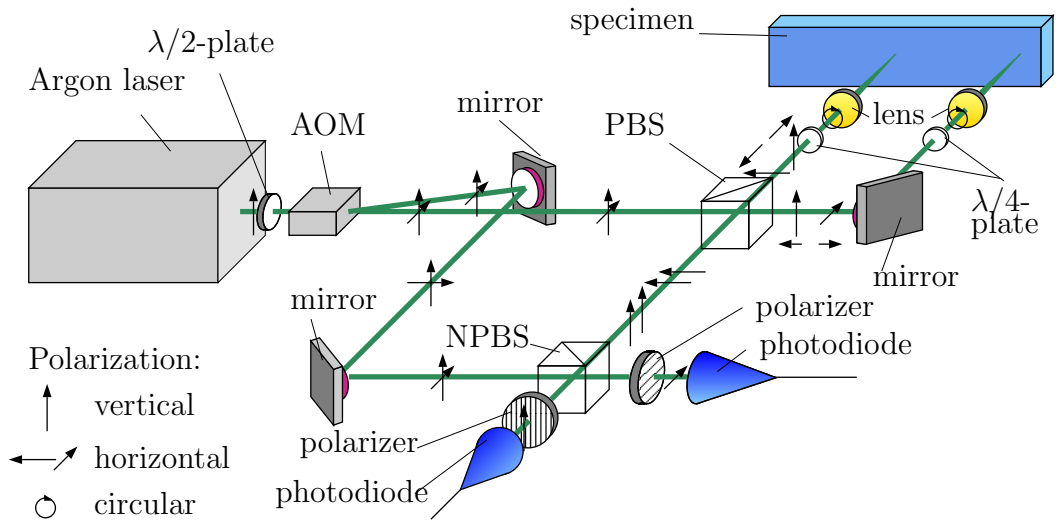

Figure 3.2: Schematic of the dual-probe interferometer.

causing this beam split, plus a frequency shift. Note that generally, a single beam is split into an infinite number of separate beams, but only two of these beams (the unshifted and the first order shifted beam) are used in the interferometer, carrying about 95 % of the power from the original beam. The frequency shifts are of integer orders of the frequency of the piezoelectric transducer — 40 MHz in this interferometer.

The object beam (unshifted) is split into horizontally and vertically polarized light at the polarizing beam splitter (PBS) — vertically polarized light is reflected, while horizontally polarized light passes through. The vertical (reflected) component of the 45° polarized light is circularly polarized by a $\lambda/4$-plate, focused by a lens and is reflected off the specimen (object) surface. On its way back, this beam is rotated from circular to horizontal polarization by the $\lambda/4$-plate, passes the PBS and hits the nonpolarized beam splitter (NPBS) — approximately half of the beam energy goes through a NPBS, while the other half is reflected at 90°. The horizontal (passing through the PBS) component of the object beam is reflected off a mirror, rotated into circularly polarized light, focused by a lens and is reflected off the specimen's surface. On its way back this beam is rotated from circular to vertical polarization

by the $\lambda/4$-plate, is reflected off the mirror and the PBS and also hits the NPBS. When the two component of the object beam reflect off the specimen surface they are frequency shifted an additional amount due to the surface velocity (Doppler effect).

After leaving the AOM, the reference beam is reflected at two mirrors and hits the NPBS where it is recombined with the two components of the object beam. After leaving the beam splitter cube, the recombined beams (reflected and transmitted at the NPBS) pass through a polarizer separating the information of both object beams and filtering the horizontally an the vertically polarized component of the recombined beam. Both filtered beams finally hit the photodiodes converting the intensity of the light into voltage signals.

3.1.3 Instrumentation

The instrumentation takes the output voltage from the photodiode, converts (demodulates) it to an absolute frequency shift and then filters and processes the signal. This setup uses an FM discriminator (see Hurlebaus [14] for details) to demodulate the voltage from the photodiode. The demodulated signal is low pass filtered with 10 MHz to reduce the noise level, afterwards discretized by an oscilloscope with a sampling frequency of 100 MHz. The oscilloscope is connected to a personal computer (PC) via GPIB.

3.1.4 Specimen

Two different specimens are considered in this research. One specimen is an aluminum 3003 *plate* which is plane, polished and has a size of 305 mm x 610 mm x 0.99 mm. The other specimen is an aluminum block, considered as half space, which is also plane, polished and has a size of (103 mm x 207 mm x 155 mm). Neither specimen has any artifical defects and note that aluminum 3003 is selected in order to be able to compare the results of this research to those of previous research like Eisenhardt [12] and Benz [3]. Finally, note that the relatively large plate size (305 mm x 610 mm) is used to minimize interference of reflections from the plate

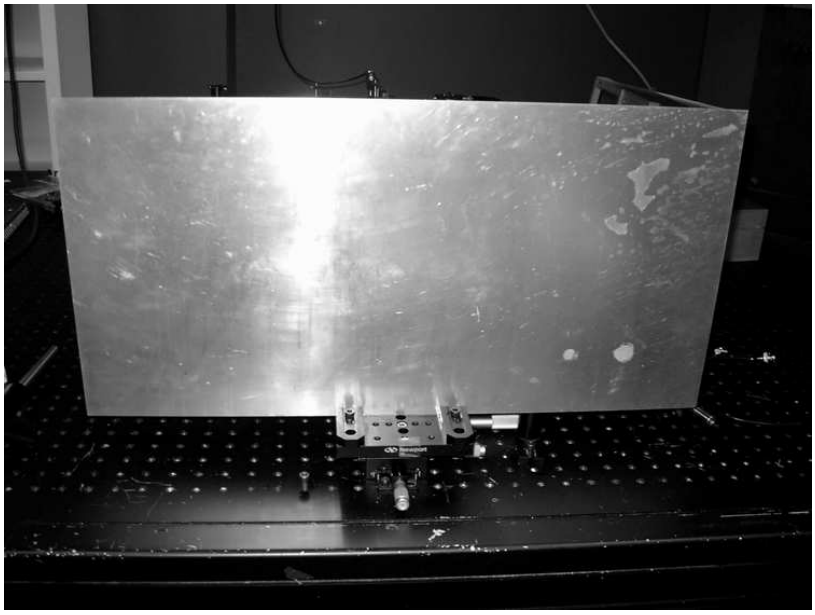

Figure 3.3: Photograph of the mounting device and plate.

edges. In later discussions the plate is considered as "infinite." This consideration can be justified by relating the relatively small source receiver distance of 46 mm to the large plate size. Furthermore, the complete set of measurements is truncated after 100 μsec so that one can demonstrate with time-of-flight calculations that there are no edge reflections in this time window. Looking at the half space geometry, the statement that boundaries and edges do not influence the measured data, does not hold anymore. Thus, reflections and their influence on the outcomes have to be analyzed carefully.

The plate is mounted in a way that the mounting process does not interfere with the propagation of the Lamb waves. This requirement is satisfied by mounting the plate lengthwise on a steel base plate. As depicted in Figure 3.3, the plate is fixed on the bottom by two metal elbows on the one side and a metal bar on the other side. The half space, shown in Figure 3.4, is simply situated on a steel plateau and attached to a stop to maintain its position during the measurements. Since the aluminum block is very heavy, no further mounting devices or attaching methods are required.

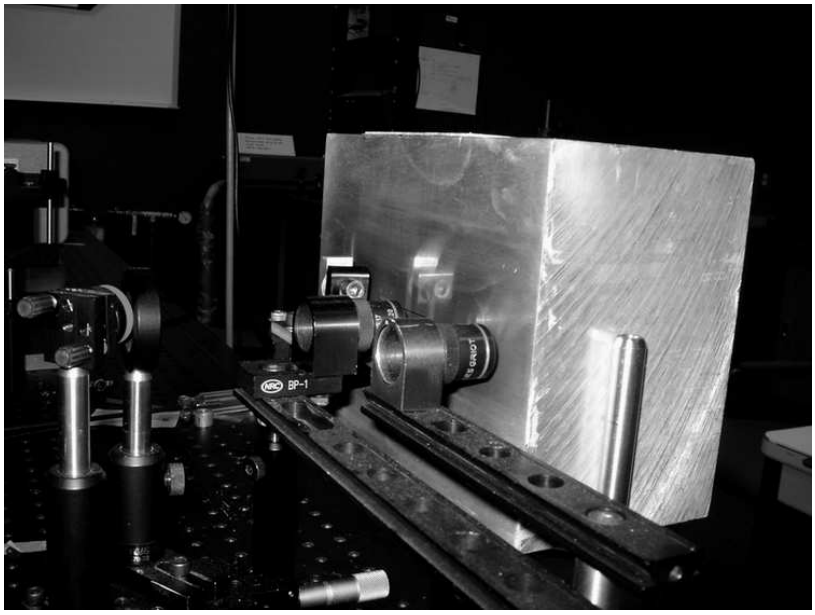

Figure 3.4: Photograph of the stop mechanism and half space.

3.2 Experiments performed

3.2.1 Measurements on the Plate

The following sets of measurements are performed on the plate:

- One set of 101 equidistant measurements (with equal step of 0.1 mm separating each measurement location) which are performed with the laser source and laser interferometric receiver on the plate (one single laser measurement is depicted in Figure 3.6, plot (a)). Both, source and receiver are aligned such that the measurement and excitation points are in the middle of the plate, and on the same side of the plate. The largest propagation distance between source and receiver is 51 mm (measurement location ♯ 1) and the shortest propagation distance is 41 mm (measurement location ♯ 101) — this data set represents a set of symmetric propagation distances centered about a propagation distance of 46 mm. This data set of measurements will be referred to as "laser source Lamb."

- One set of measurements on the plate performed with the commercial transducer (*Panametrics V544*) source and the laser interferometer (described in Section 3.1.2) as receiver (source and receiver on the same side of the plate). All the couplants mentioned in Section 3.1.1.2 are tested, but the food oil gave the most repeatable performance and it will be used in all the future commercial transducer measurements. The commercial transducer source is placed on the plate surface such that its center is located 46 mm away from the (point) laser receiver. This measurement will be referred to as "transducer source Lamb" (Figure 3.6, plot (b)).

- One set of measurements on the plate performed with the glued piezo disc source (described in Section 3.1.1.2) and the same laser interferometric receiver (source and receiver again on the same side of the plate). The piezo disc is placed on the plate surface such that its center is located 46 mm away from the (point) laser receiver. This measurement will be referred to as "piezo source Lamb" (Figure 3.6, plot (c)).

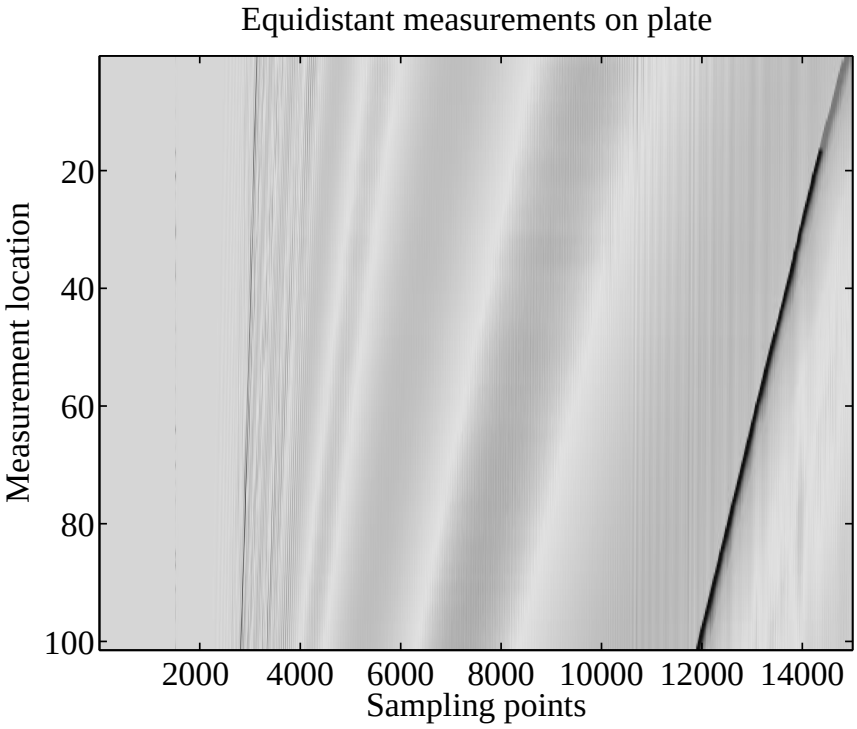

Figure 3.5: Image of the plate measurement set.

Figure 3.5 is a graphical summary of all 101 laser source Lamb measurements, while Figure 3.6 are (top-to-bottom) a representative laser source Lamb (propagation distance of 46 mm), the transducer source Lamb, and the piezo source Lamb signals. The vertical axis of the image in Figure 3.5 corresponds to the measurement locations, from ♯ 1 (propagation distance of 51 mm) at the top to ♯ 101 (propagation distance of 41 mm) at the bottom. Note that the laser source Lamb measurements are each driven with a pre-trigger of 1500 sampling points (15 μsec) — one can see a very fine line or a peak at 1500 points (0 μsec) which corresponds to the electromagnetic noise of the generation instrumentation in both Figures 3.5 and 3.6. There is also a very thick line between 12000 (105 μsec) and 15000 (135 μsec) points in Figure 3.5 that is caused by the acoustic air-pulse of the laser source. This peak does not occur for the piezoelectric sources, since they do not emit an acoustic air-pulse. Looking at Figure 3.5 one can detect that the earliest arrival time (for measurement ♯ 101) of the Lamb waves is after 1000 points (10 μsec), excluding the pre-trigger. Moreover, there is a very pronounced low frequency component in the Lamb wave after 4000 points (25 μsec).

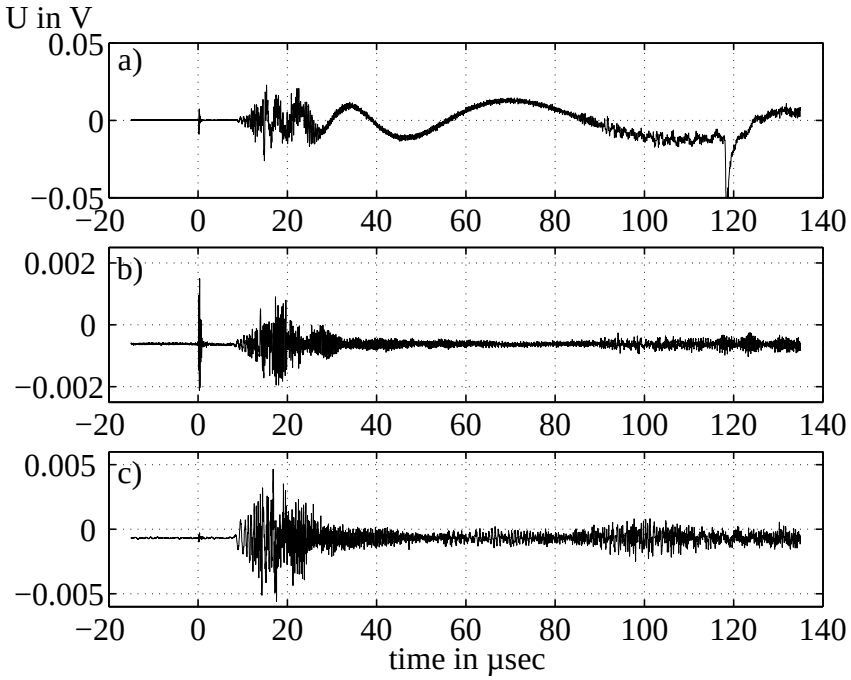

Figure 3.6: Measurement sets on the plate.

3.2.2 Measurements on the Half Space

The following sets of measurements are performed on the half space:

- One set of 101 equidistant measurements (with equal step of 0.1 mm separating each measurement location) which are performed with the laser source and laser interferometric receiver on the half space (one single laser measurement is depicted in Figure 3.8, plot (a)). Both, source and receiver are aligned such that the measurement and excitation points are in the middle of the half space. The furthest propagation distance between source and receiver is 51 mm (measurement location ♯ 1) and the shortest propagation distance is 41 mm (measurement location ♯ 101) — this data set represents a set of symmetric propagation distances centered about a propagation distance of 46 mm. For further considerations, this set of measurements will be referred to as "laser source Rayleigh".

- One set of measurements on the half space performed with the commercial transducer (*Panametrics V544*) source and the laser interferometer (described in Section 3.1.2) as receiver. All the couplants mentioned in Section 3.1.1.2 are tested, but the food oil gave the most repeatable performance and it will be used in all the future commercial transducer measurements. The commercial transducer source is placed on the half space surface such that its center is located 46 mm away from the (point) laser receiver. This measurement will be referred to as "transducer source Rayleigh" (Figure 3.8, plot (b)).

- One set of measurements on the half space with the glued piezo disc source (described in Section 3.1.1.2) and the same laser interferometric receiver. The piezo disc is placed on the half space surface such that its center is 46 mm away from the (point) laser receiver. This measurement will be referred to as "piezo source Rayleigh" (Figure 3.8, plot (c)).

Figure 3.7 is a graphical summary of all 101 laser source Rayleigh measurements, while Figure 3.8 are (top-to-bottom) a representative laser source Rayleigh (propagation distance of 46 mm), the transducer source Rayleigh and the piezo source

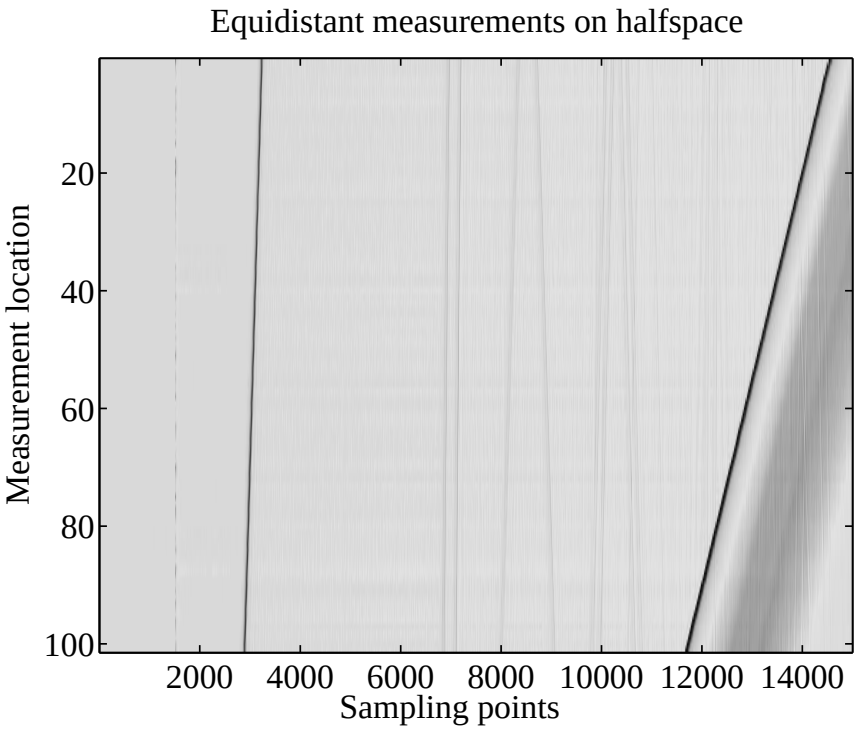

Figure 3.7: Image of the half space measurement set.

Rayleigh signals. The vertical axis of the image in Figure 3.7 corresponds to the measurement locations, from ♯ 1 (propagation distance of 51 mm) at the top to ♯ 101 (propagation distance of 41 mm) at the bottom. Note that the laser source Rayleigh measurements are each driven with a pre-trigger of 1500 sampling points (15 μsec) — one can see a very fine line or a peak at 1500 points (0 μsec) which corresponds to the electromagnetic noise of the generation instrumentation in both Figures 3.7 and 3.8. One significant feature in Figure 3.7 is the arrival of the Rayleigh wave after approximately 1500 points (15 μsec), excluding the pre-trigger. All visible lines after 6000 points (45 μsec) are representations of reflections on the half space boundaries. The very thick line between 12000 (105 μsec) and 15000 points (135 μsec) in Figure 3.7 is again caused by the acoustic air-pulse of the laser source. Table 3.1 summarizes and shows all the measurement sets performed and provided in this research.

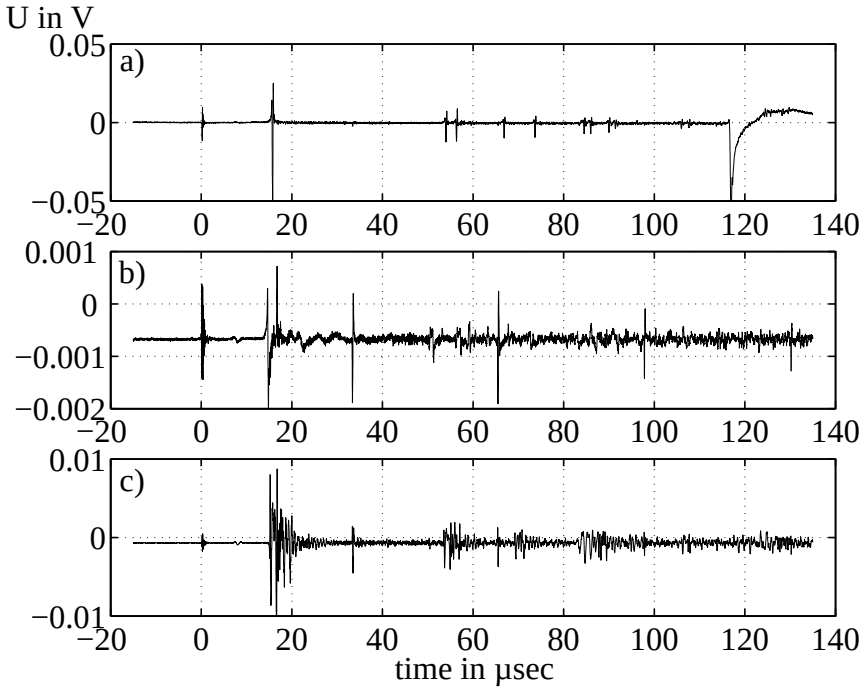

Figure 3.8: Measurement sets on the half space.

Table 3.1: Summary of measurement sets

name	specimen	source	receiver
laser source Lamb	plate	laser	laser interferometer
transducer source Lamb	plate	commercial transducer	laser interferometer
piezo source Lamb	plate	piezo disc	laser interferometer
laser source Rayleigh	half space	laser	laser interferometer
transducer source Rayleigh	half space	commercial transducer	laser interferometer
piezo source Rayleigh	half space	piezo disc	laser interferometer

3.2.3 Propagation Distance Errors

Note that for the following discussions, propagation distance errors have to be taken into consideration. For the laser source Rayleigh and the laser source Lamb measurement sets, a micrometer screw was used to set the equidistant locations of the excitation points. The accuracy of the used micrometer is in the range of $\pm$ 0.005 mm. The propagation distance error for the measurements performed with the piezo disc and the transducer depends on two features:

- The actual effective surface of the piezo disc or the transducer
- The actual position of the center point of the piezo disc or the transducer

Inspections in Chapter 5 will show that the propagation distance error due to these two features is below $\pm$ 0.1 mm.

CHAPTER 4

The Source Function Approach

4.1 Motivation

Previous research results (e.g. Benz et al. [4]) have shown that it is possible to obtain accurate dispersion curves for plates using a laser source for the wave excitation. The point nature and broad bandwidth of the laser source means that the individual modes in the dispersion curves are well separated and are clearly distinguishable, especially for a frequency band from 500 kHz through 5 MHz [4] for the used excitation - and measurement system. If the dispersion curves can be accurately measured, then there is quantitative information about the behavior of the individual modes. Each mode interacts with the specimen and especially its defects, so that one can detect and even characterize certain material properties and defects using these dispersion curves. When examining a similar measurement — one made with either a piezoelectric source (referred to as a "piezo disc") or a commercial transducer(referred to as a "transducer"), instead of a laser source — one recognizes a tremendous loss in information. The dispersion curves developed using a piezoelectric source (or a transducer) are blurred (some modes are not even excited), making it difficult to distinguish between different modes, and complicating any conclusions about structural health. The motivation of this portion of the research is to develop a methodology to describe the effects of transducer and piezo disc sources (when compared to the laser source), then extract the effect of these transducer and piezo disc sources, and finally compensate for the negative influence of these sources — the ultimate goal is to obtain dispersion curves close to those developed with an "ideal" laser signal. Comparing the practicability, costs and sensitivity of transducers or piezo discs with laser sources, this methodology would have a positive impact in structural health

monitoring.

4.2 Temporal and Spatial Effects: Forward Modeling

4.2.1 Model

A scheme of the source - receiver location is depicted in Figure 4.1. It shows the location of a source distributed over a region of the surface S with a spatial extent described by vector $\mathbf{r}'$ and the location of the receiver described by vector $\mathbf{r}$.

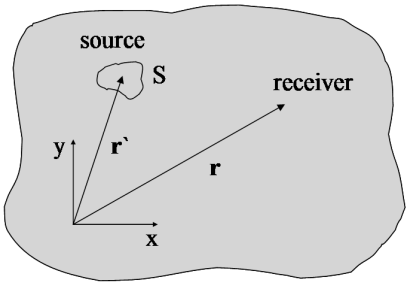

Figure 4.1: Scheme of source - receiver location.

The continuous representation of the equation which is subject to the further considerations can be written as follows:

$$x(\mathbf{r},t) = s(t) * \int_S w(\mathbf{r}')G(\mathbf{r},\mathbf{r}',t)\mathrm{d}S \tag{4.1}$$

where $w(\mathbf{r}')$ represents the weight for the Green's function obtained at $\mathbf{r}$ (excited at $\mathbf{r}'$). The effects of the source are captured in the source time function $s(t)$. In this research the set of laser source signals $x_{\mathrm{LSR}_j}(n)$ corresponds to the single Green's functions (at different locations j) and the measured transducer signal $x_{\mathrm{TR}}(n)$ is described by x. Thus, the continuous representation (Equation (4.1)) can be rewritten to the discrete representation in Equation (4.2).

$$x_{\mathrm{TR}}(n) = s(n) * \sum_j w_j x_{\mathrm{LSR}_j}(n) \tag{4.2}$$

The following sections consider the two most intuitive physical influences of a piezo disc or transducer on signal quality: temporal effects and spatial effects; that is, the influence of $s(n)$ and w_j are subject of the following discussions.

4.2.2 Temporal Effects

Consider the temporal effects using a synthetic source function (Figure 4.2(b)) $s(n)$ only that models the possible temporal influence with exponentially damped oscillations of the transducer. This synthetic source function is convolved with a single laser source measurement to obtain the contour plot depicted in Figure 4.2(c) — only one w in Equation (4.2). This figure confirms that a simple oscillation of the source has simply filtered the time-frequency laser representation of the signal in Figure 4.2(a). This makes physical sense by noting that a convolution of a weighted sine function with an arbitrary signal in the time domain is simply a filtering operation. This filtering can be more clearly seen by looking at the synthetic source function in the frequency domain. Figure 4.2(d) shows that a peak is developed at 2.75 MHz, which corresponds to the simulated input frequency of the modeled source. Note that the oscillations in the peripheral areas of the main lobe are due to the sharp cutoff of the synthetic source function after 4 periods. This effect would not be present in a real piezo source, since the temporal oscillations would die out smoothly. Recalling that a convolution in the time domain corresponds to a multiplication in the frequency domain, one can obtain the plot in Figure 4.2(c) by simply multiplying each horizontal line of the plot in Figure 4.2(a) with the FFT of the synthetic source, shown in Figure 4.2(d).

This demonstrates that one does not have to model temporal effects in order to recover dispersion curves but the bandwidth of the source function must be sufficient in order to recover the modes of interest.

4.2.3 Spatial Effects

Next consider the spatial influence of the transducer. To do this, examine the Fourier transformed transducer source Lamb signal and the Fourier transform of a

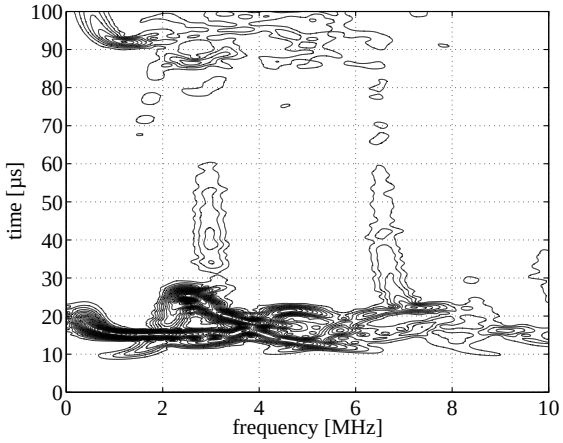

(a) STFT contour plot of perfect laser signal.

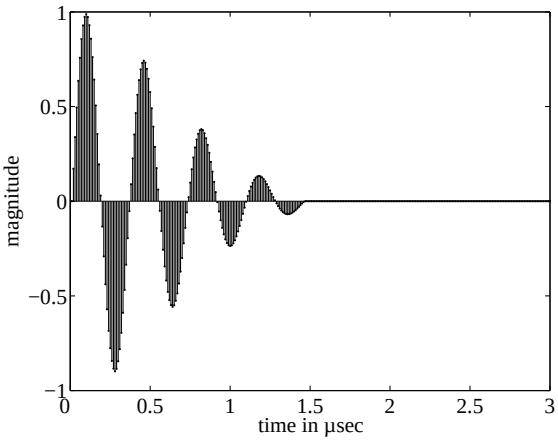

(b) Time domain plot of synthetic source function.

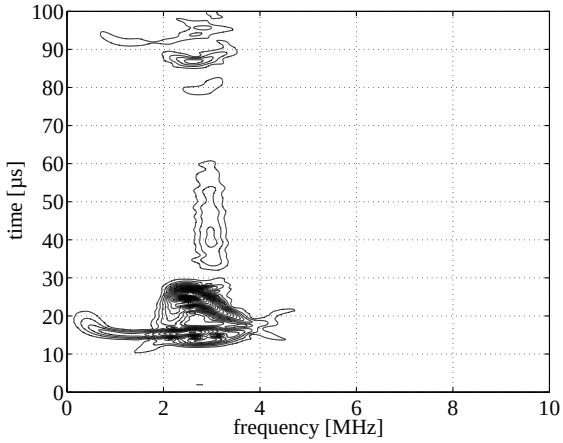

(c) STFT contour plot of convolved laser signal.

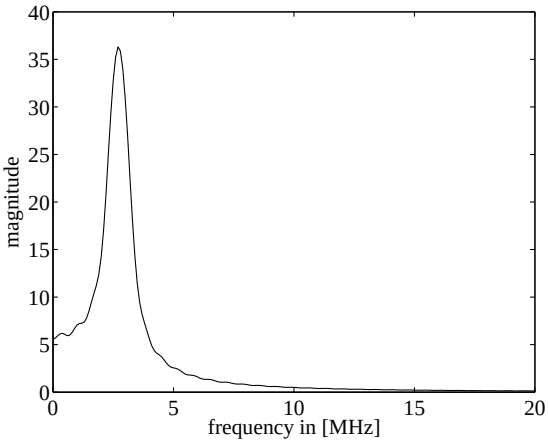

(d) Frequency domain plot of synthetic source function.

Figure 4.2: Plots for temporal effect discussion.

laser source Lamb signal. As shown in Figure 4.3(a) and Figure 4.3(b), there are conspicuous differences in the frequency content of the two signals. Hence it is attempted to model the spatial extend of a piezo disc or a transducer by averaging laser source signals of different locations (on a distance corresponding to the effective transducer diameter). Then compare the result of the averaged laser source signals and the transducer signal to verify that the basic features of the transducer signal are modeled by averaging single laser source signals. Therefore take advantage of the laser source Lamb set by averaging 61 of the measurement points around the center and weight each of these points so that the entire set has the shape of a Gaussian window. Note that for this case only a line source is modeled, even though the transducer is an area source. The plot of the Fourier transform of the averaged signal is shown in Figure 4.3(c). Figure 4.3(d), which is a contour plot of the averaged laser source signal, indicates that spatial averaging distorts the dispersion curves. Compared to Figure 4.2(a), note a tremendous loss in separation between the single dispersion curves for times below 30 μsec.

All the signals in Figure 4.3 are 5 MHz low pass- and 500 kHz high pass filtered. Note that there is a very pronounced frequency peak between 3 - and 4 MHz for the transducer source signal of Figure 4.3(b) which is poorly developed in the single laser source signal of Figure 4.3(a). The existence of this peak in the averaged laser source signal shows that even a line source model (with single laser source signals) is suitable to model the basic feature of the transducer signal (3 MHz peak). Even though one cannot immediately say that it is possible to resolve the spatial effects of the piezo disc or transducer sources by just averaging laser signals, this approach seems to be promising in terms of an expansion of the model.

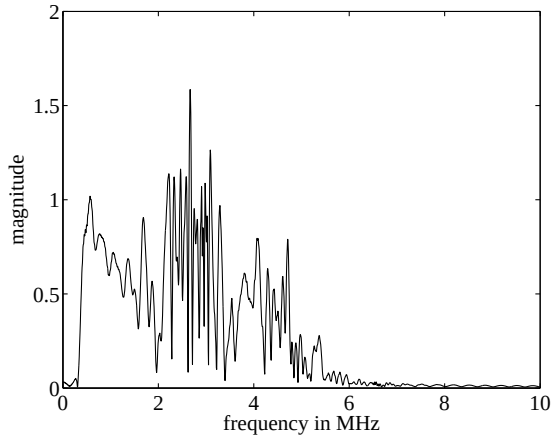

(a) FFT of a single laser source Lamb signal.

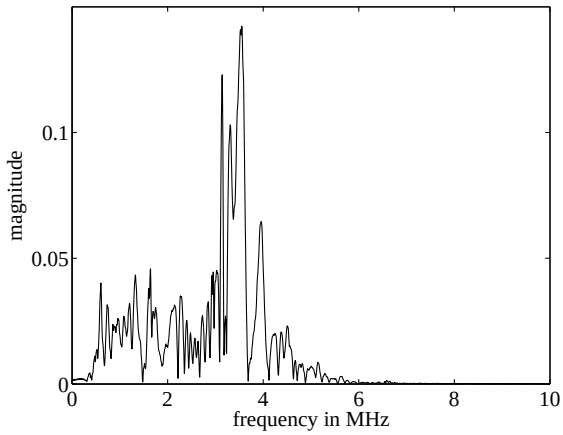

(b) FFT of the transducer source Lamb signal.

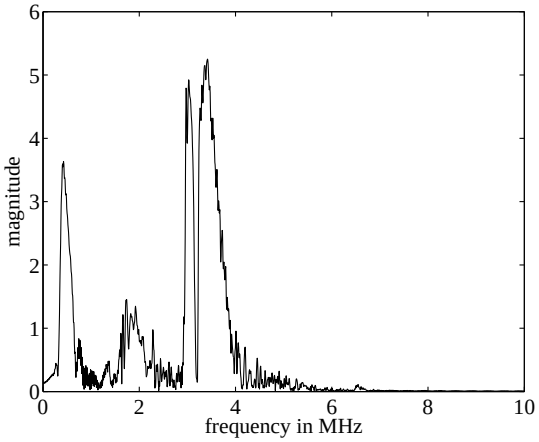

(c) FFT of an averaged laser source Lamb signal with Gaussian window.

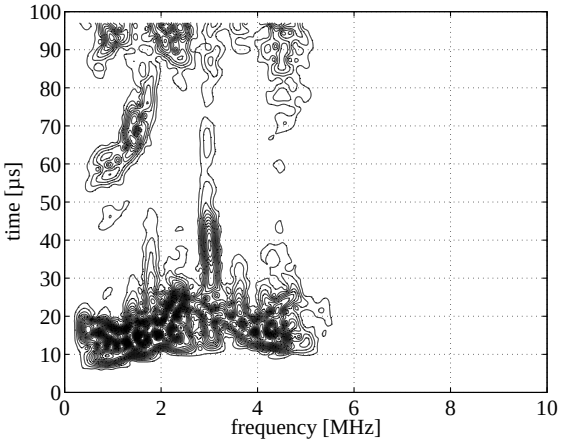

(d) Contour plot of the averaged laser source Lamb signal.

Figure 4.3: Plots for averaging effect.

Therefore, a detailed discussion on how to select and calculate the weights in an optimal sense is presented in Section 4.3.2.

4.3 Time Domain Deconvolution Theory

Consider a methodology to recover time domain source functions by deconvolution. Generally, convolution integrals arise in many physical systems where the principle of superposition can be applied. In elastic wave propagation problems, the concept of a Green's function leads directly to a time-domain convolution integral. In linear systems theory, the concept of an impulse response, which is a Green's function with

only time as a variable, also results in a convolution integral. Hence, many wave propagation phenomena and linearly superposed effects on the waves can be modeled by multiple convolution integrals. This model can be generally written as

$$\begin{aligned} v(t) = \int_{-\infty}^{\infty} \mathrm{d}t_{n-1} x_n(t - t_{n-1}) \int_{-\infty}^{\infty} \mathrm{d}t_{n-2} x_{n-1}(t_{n-1} - t_{n-2}) \\ \cdots \int_{-\infty}^{\infty} \mathrm{d}t_2 x_3(t_3 - t_2) \int_{-\infty}^{\infty} \mathrm{d}t_1 x_2(t_2 - t_1) x_1(t_1) \end{aligned} \tag{4.3}$$

Equation (4.3) can also be rewritten to Equation (4.4) in the convolution operator ($*$) representation

$$v(t) = x_1(t) * x_2(t) * \cdots * x_n(t) \tag{4.4}$$

Hence, $v(t)$ can be simply evaluated by convolving the x_i's. The inverse problem of finding x_j from $v(t)$ and the remaining x_i's is called time domain deconvolution. It is basically the procedure of solving an integral equation of the form

$$v(t) = \int_{-\infty}^{\infty} x_1(\tau) x_2(t - \tau) \mathrm{d}\tau \tag{4.5}$$

where $x_2(t)$ is the unknown component. See Michaels [18] for detailed information about deconvolution methods and their applications. Other researchers like Ching et al. [8], investigate additional approaches to time domain deconvolution.

Due to the sampling with a sampling interval ΔT and n samples per measurement, digitized signals are only available in discrete form. Thus, introduce the discrete convolution

$$v(n) = \sum_{m=-\infty}^{\infty} x_1(m) x_2(n - m) \tag{4.6}$$

which can also be written as

$$v(n) = x_1(n) * x_2(n). \tag{4.7}$$

Renaming the signals in Equation (4.7) into ones more meaningful variables for the work here, one can define

$$x_{\mathrm{TR}}(n) = x_{\mathrm{LSR}}(n) * s(n), \tag{4.8}$$

where x_{TR} denotes the "transducer source" signal and x_{LSR} is a single signal of the "laser source" set. Now, deconvolution problem in Equation (4.8) is solved to obtain the source function $s(n)$. Considering the laser source as a "perfect source", the source function would be a mathematical construct which is physically meaningful, and enables interpretation of $s(n)$. Ideally, $s(n)$ is a mathematical representation of the oscillations and mechanical influences of the transducer only.

Assuming that $s(n)$ is causal — it represents a real world process — one can solve Equation (4.8) directly by factoring a polynomial of degree N. This method can be seen by expanding the summation in Equation (4.8) to

$$\begin{aligned} x_{\mathrm{TR}}(0) &= x_{\mathrm{LSR}}(0)\ s(0) \\ x_{\mathrm{TR}}(1) &= x_{\mathrm{LSR}}(0)\ s(1) + x_{\mathrm{LSR}}(1)\ s(0) \\ x_{\mathrm{TR}}(2) &= x_{\mathrm{LSR}}(0)\ s(2) + x_{\mathrm{LSR}}(1)\ s(1) + x_{\mathrm{LSR}}(2)\ s(0) \\ &\vdots \end{aligned} \tag{4.9}$$

which yields an exact solution of the general form

$$s(n) = [x_{\mathrm{TR}}(n) - \sum_{m=1}^{n} x_{\mathrm{LSR}}(m) s(n-m)] \frac{1}{x_{\mathrm{LSR}}(0)}. \tag{4.10}$$

This method, referred to as "direct solution", although simple to implement is numerically unstable and leads to exponentially increasing solutions (for details see Michaels [18]).

4.3.1 Least Squares Deconvolution

4.3.1.1 Toeplitz Recursion

The least squares deconvolution approach is a method to approximate the exact solution in the least squares sense by minimizing the mean square error between the desired and actual convolution output. Robinson and Treitel [29] described this approximation which will from now on be called $\hat{x}_{\mathrm{TR}}$. The approximation procedure

and an outline of how to solve it, is presented in [18]. Writing Equations (4.9) in matrix form and assuming that x_{LSR} is of length N, the following matrix equation can be obtained:

$$\begin{pmatrix} x_{\mathrm{LSR}}(0) & 0 & \dots & 0 \\ x_{\mathrm{LSR}}(1) & x_{\mathrm{LSR}}(0) & 0\dots & 0 \\ \vdots & & & 0 \\ x_{\mathrm{LSR}}(N-1) & \dots & \dots & x_{\mathrm{LSR}}(0) \\ 0 & x_{\mathrm{LSR}}(N-1) & \dots & x_{\mathrm{LSR}}(N-1-M) \\ \vdots & 0 & & \vdots \\ \vdots & \vdots & 0 & x_{\mathrm{LSR}}(N-1) \end{pmatrix} \begin{pmatrix} s(0) \\ s(1) \\ . \\ . \\ s(M-1) \end{pmatrix} = \begin{pmatrix} \hat{x}_{\mathrm{TR}}(0) \\ \hat{x}_{\mathrm{TR}}(1) \\ . \\ . \\ . \\ \hat{x}_{\mathrm{TR}}(N+ \\ M-2) \end{pmatrix} \tag{4.11}$$

Note that the approximation $\hat{x}_{\mathrm{TR}}$ is of length $N+M-1$. Equation (4.11) can be represented as

$$\tilde{A}S = B \tag{4.12}$$

where

$$A_{ij} = \begin{cases} 0 & i < j \\ 0 & i - j \geq N \\ x_{\mathrm{LSR}}(i-j) & otherwise. \end{cases}$$

The comprehensive task at this point is to find the optimal s. Since the method to find s is an approximation, the recovered s is actually a $\hat{s}$ but for simplicity reasons it will still be called the source function s. To minimize the error Err between $\hat{x}_{\mathrm{TR}}$ and x_{TR}, start out with the following equation

$$Err = \sum_{n=0}^{N+M-2} [x_{\mathrm{TR}}(n) - \hat{x}_{\mathrm{TR}}(n)]^2 \tag{4.13}$$

Defining the vector $\hat{X}_{\mathrm{TR}}$ as

$$\hat{X}_{\mathrm{TR}} = \hat{x}_{\mathrm{TR}}(i-1),$$

Equation (4.13) can be represented in matrix form as

$$Err = (\tilde{A}S - \hat{X}_{\mathrm{TR}}) \cdot (\tilde{A}S - \hat{X}_{\mathrm{TR}}) \tag{4.14}$$

The error in Equation (4.14) becomes in subscript notation

$$Err = (a_{ij}s_j - \hat{x}_{\mathrm{TR}_i})(a_{ik}s_k - \hat{x}_{\mathrm{TR}_i})$$

Minimizing the error in least squares sense with respect to each s_n means taking the partial derivatives of Err with respect to s_n and setting them to zero.

$$\begin{aligned}
\frac{\partial Err}{\partial s_n} &= 0 \\
&= \frac{\partial}{\partial s_n}(a_{ij}s_j - x_{\mathrm{TR}_i})(a_{ik}s_k - x_{\mathrm{TR}_i}) \\
&= (a_{ij}s_j - x_{\mathrm{TR}_i})a_{in} + (a_{ik}s_k - x_{\mathrm{TR}_i})a_{in} \\
&= 2\,(a_{ij}s_j - x_{\mathrm{TR}_i})a_{in} = 0
\end{aligned} \tag{4.15}$$

This can again be written in matrix form as

$$\tilde{A}^T\tilde{A}S = \tilde{A}^T X_{\mathrm{TR}},$$

where define a matrix $\tilde{R}$ and a vector G to be

$$\begin{aligned}
R &= \tilde{A}^T\tilde{A} \\
G &= \tilde{A}^T X_{\mathrm{TR}}.
\end{aligned}$$

Note that now

$$\tilde{R}S = G \tag{4.16}$$

has to be solved, where

$$R_{ij} = \begin{cases} \sum_{m=0}^{N-1-(i-j)} x_{\mathrm{LSR}}(m+i-j)x_{\mathrm{LSR}}(m) & i \geq j \\ R_{ij} & i < j \end{cases} \tag{4.17}$$

is the $(i-j)^{\mathrm{th}}$ term of the autocorrelation of $x_{\mathrm{LSR}}(n)$ and

$$G_i = \sum_{m=0}^{N-1} x_{\mathrm{LSR}}(m)x_{\mathrm{TR}}(m+i) \tag{4.18}$$

is the i^{th} term of the cross-correlation between $x_{\mathrm{LSR}}(n)$ and $x_{\mathrm{TR}}(n)$.

Solving the system of Equations (4.16) is in general a very computationally intensive task. However, if it is assumed that $x_{\mathrm{LSR}}(n)$ and $x_{\mathrm{TR}}(n)$ are both finite length signals of length N, then the autocorrelation matrix $\tilde{R}$ is in Toeplitz form and can be solved by a very efficient method, known as Toeplitz recursion. Even though this assumption is not generally correct, it can provide a good approximation if the signals of interest have decayed sufficiently within the recorded time windows. Detailed information about the Toeplitz recursion can be found in [29].

4.3.1.2 Improved Toeplitz Recursion

The effect of the finite length of the signals on the performance of the Toeplitz recursion algorithm and a method of compensation is presented. For mathematical simplicity, assume the signals are continuous in time, and $x_{\mathrm{TR}}(t)$, $x_{\mathrm{LSR}}(t)$ and $s(t)$ are defined. A major problem is the fact that the signals x_{TR} and x_{LSR} are not of finite length, although the measured data is of finite length. This results in an artificial transition between the non-zero and zero parts in the matrix of Equation (4.11). Note that the Toeplitz recursion is designed for matrices in Toeplitz form. Since the signals are of finite length, this forced sharp cutoff between signal and zeros makes the calculated autocorrelation and cross-correlation inaccurate for values around this transition. To avoid this sharp cutoff, the basic idea is to shape the signals with an exponential window to smooth out the transition and thus make the correlations more accurate. Therefore, consider the standard deconvolution problem, but now in continuous time representation,

$$\begin{aligned} \tilde{x}_{\mathrm{TR}} &= x_{\mathrm{LSR}}(t) * s(t) \\ &= \int_0^t x_{\mathrm{LSR}}(\tau) s(t-\tau) \mathrm{d}\tau. \end{aligned} \tag{4.19}$$

Multiplying both signals on the right hand side in Eg. (4.20) by an exponential window, yields the following expression:

$$\int_0^t x_{\mathrm{LSR}}(\tau) e^{-\alpha\tau} s(t-\tau) e^{-\alpha(t-\tau)} \mathrm{d}\tau$$

Rearranging this expression as shown below, one can obtain a very useful result:

$$\begin{aligned}\int_0^t x_{\mathrm{LSR}}(\tau)e^{-\alpha t}s(t-\tau)\mathrm{d}\tau &= e^{-\alpha t}\int_0^t x_{\mathrm{LSR}}(\tau)s(t-\tau)\mathrm{d}\tau \\ &= e^{-\alpha t}\tilde{x}_{\mathrm{TR}} \end{aligned} \tag{4.20}$$

Thus, exponentially windowing the two signals prior to convolution yields the same signal as exponentially windowing the result. The property of Equation (4.20) can be used to ensure that the signals x_{LSR} and x_{TR} meet the length requirements necessary for using Toeplitz recursion. The exponential window (the decay) is shaped by the shaping parameter α. An appropriate value for α is simply selected such that $x_{\mathrm{LSR}}(n)$ has decayed to essentially zero by N points, and window both, x_{LSR} and x_{TR} by $e^{-\alpha n\Delta T}$ to obtain the desired source function. This technique is more powerful then traditional windowing methods, since there are no approximations involved due to this convolution property of an exponential window.

Figure 4.4 depicts a direct comparison between Toeplitz recursion without applying the windowing "trick" (Figure 4.4(a), 4.4(c) and 4.4(e)), and the Toeplitz recursion with the procedure presented in Equation (4.20) (Figure 4.4(b), 4.4(d) and 4.4(f)). To verify this procedure, a numerical source function is implemented and convolved with the measured laser source signal in Figure 4.4(a), which is used as the impulse response, to represent the measured piezo disc signal (Figure 4.4(c)). Now, to check the functionality of the Toeplitz recursion without any modifications, a deconvolution with the known impulse response and the piezo source signal to recover the source function is performed. As shown in Figure 4.4(e), there is a significant difference between the original and the recovered source functions, particularly at longer times due to the length approximation of the Toeplitz recursion.

If the same steps are performed, but now by windowing the impulse response and the measured signal with an exponential, the performance significantly improves. That means, if one deconvolves the theoretical source function with the windowed impulse response in Figure 4.4(b) to get the measured signal in Figure 4.4(d), one

obtains a recovered source function which is essentially the same as the theoretical one (Figure 4.4(f)). However, consider the fact that due to the windowing of the signals, some amplitude information is lost for longer times in the impulse response and in the measured signal. But, as depicted in the comparison of the two source functions, this effect does not play a mayor role in recovering the source function. Furthermore, considering the Lamb wave of Figure 4.4(a), most of the key information is contained in the first 10 - 15 μsec. As seen in Figure 4.4 the exponential window has significantly reduced the signal amplitudes past about 15 - 20 μsec. If the case that the windowing cuts off too much of the signal, there is the possibility to adjust α in Equation (4.20) appropriately. Note that before comparing between the two source functions, the recovered source function has to be un-windowed. This is easily done by multiplying it with the inverse of the exponential function used to window the impulse response.

4.3.1.3 Deconvolution of Noisy Signals

Since one must deal with measured data, noise is superimposed on the actual information. To take care of the noise, a simple modification is made in the algorithm of the Toeplitz recursion. This modification is made on the basis of the discussions about deconvolution in the presence of noise by Robins [28]. As mentioned earlier, the calculation of the autocorrelation matrix is the basic operation in the algorithm. Thinking of noise as unpredictable superimposed information, one can modify the initial value for the calculation of the autocorrelation. This is done by estimating the signal-to-noise ratio and adding it to the initial value. Note that the autocorrelation is calculated as shown in Equation (4.21).

$$R_f(t) = \lim_{T\to\infty} \frac{1}{2T} \int_{-T}^{T} f(\tau) f(t+\tau) \mathrm{d}\tau \tag{4.21}$$

To explain why one must modify the initial value, first consider a white noise signal. The autocorrelation of this signal is zero for all values, except for a shift of zero. At this point, the autocorrelation is infinite since the two signals are identical. Since one does not deal with white noise, all the other values are non-zero, but one can conclude from this white noise scenario that the most crucial autocorrelation value to describe the influence of noise is the one at zero shift.

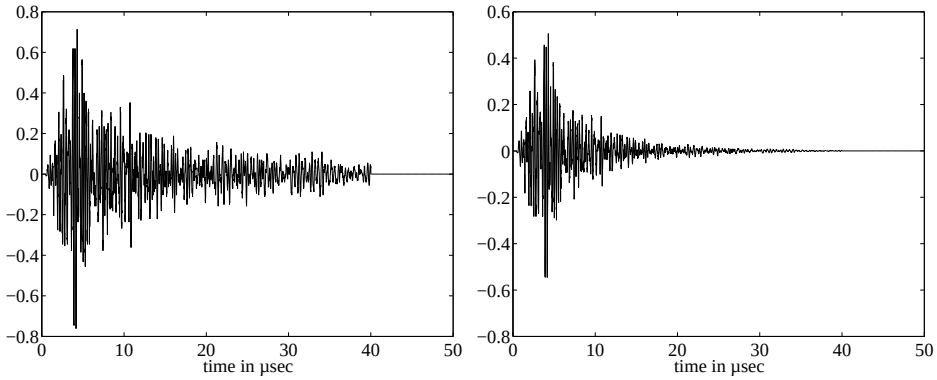

(a) Measured laser signal $x_{\mathrm{LSR}}(n)$.

(b) Exp. windowed laser signal $x_{\mathrm{LSR}}(n)e^{-\alpha n\Delta T}$.

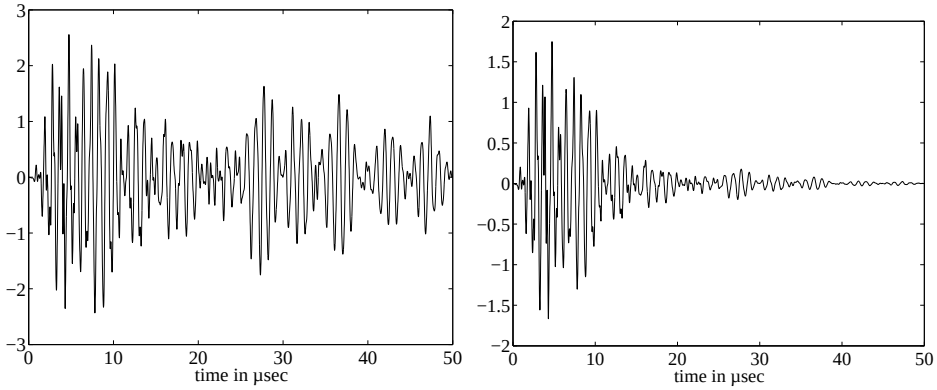

(c) Calculated transducer signal $x_{\mathrm{TR}}(n)$.

(d) Exp. windowed transducer signal $x_{\mathrm{TR}}(n)e^{-\alpha n\Delta T}$.

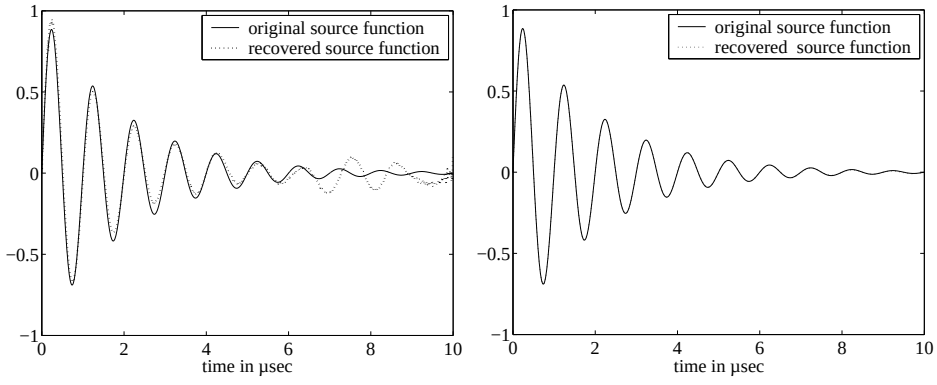

(e) Comparison of source functions regular Toeplitz.

(f) Comparison of source functions improved Toeplitz.

Figure 4.4: Plots for Toeplitz improvement discussion.

4.3.2 Spatial Inversion

Now, the piezo disc or transducer signal is to be modeled as a weighted sum of laser source signals convolved with a source time function (as written in Equation (4.2)). This section determines how to calculate optimal weights for their corresponding Green's functions in a sense of physical interpretability — so that the means squared error between measured and recovered signal (x_{TR} and $\hat{x_{\mathrm{TR}}}$) is minimized. Therefore consider Equation (4.22), which gives a representation of the measured piezo disc or transducer signal as a weighted sum of single laser source signals.

$$\hat{x}_{\mathrm{TR}}(n) = [\sum_{j=1}^{M} w_j x_{\mathrm{LSR}_j}(n)] * s(n) \tag{4.22}$$

Note that w_j is the weight applied to the j^{th} laser source signal and the source time function $s(n)$ is assumed to be known. One can optimize the fitting of the measured and recovered piezo disc (or transducer) signal by minimizing the least square error between the two signals.

$$\begin{aligned} Err &= \sum_{n=1}^{N} [\hat{x}_{\mathrm{TR}}(n) - x_{\mathrm{TR}}(n)]^2 \\ &= \sum_{n=1}^{N} [\sum_{j=1}^{M} w_j \underbrace{x_{\mathrm{LSR}_j}(n)] * s(n)}_{=q_j(n)} - x_{\mathrm{TR}}(n)]^2 \\ &= \sum_{n=1}^{N} [\sum_{j=1}^{M} w_j q_j(n) - x_{\mathrm{TR}}(n)]^2 \end{aligned} \tag{4.23}$$

To optimize the weights, take the first derivative with respect to the k^{th} weight and set it to zero.

$$\begin{aligned} \frac{\partial Err}{\partial w_k} &= \sum_{n=1}^{N} 2 \cdot [\sum_{j=1}^{M} w_j q_j(n) - x_{\mathrm{TR}}(n)] \sum_{j=1}^{M} q_k(n) \\ 0 &= \sum_{n=1}^{N} 2 \cdot [\sum_{j=1}^{M} w_j q_j(n) - x_{\mathrm{TR}}(n)] q_k(n) \\ 0 &= \sum_{n=1}^{N} [\sum_{j=1}^{M} w_j q_j(n) q_k(n) - x_{\mathrm{TR}}(n) q_k(n)] \end{aligned} \tag{4.24}$$

Rearranging the summations in Equation (4.24), Equation (4.25) is obtained. This equation is written so that the weights are decoupled from the summation over n.

$$\begin{aligned}\sum_{n=1}^{N} x_{\mathrm{TR}}(n)q_k(n) &= \sum_{n=1}^{N}\sum_{j=1}^{M} w_j q_j(n)q_k(n) \\ &= \sum_{j=1}^{M} w_j \sum_{n=1}^{N} q_j(n)q_k(n) \end{aligned} \tag{4.25}$$

Representing Equation (4.25) in matrix form, a set of matrices is obtained which is very convenient in terms of implementation purposes.

$$\underbrace{\begin{pmatrix} \sum_{n=1}^{N} q_1(n)q_1(n) & \cdots & \sum_{n=1}^{N} q_M(n)q_1(n) \\ \vdots & \ddots & \\ \sum_{n=1}^{N} q_1(n)q_M(n) & \cdots & \sum_{n=1}^{N} q_M(n)q_M(n) \end{pmatrix}}_{\mathbf{Q}} \begin{pmatrix} w_1 \\ \vdots \\ w_M \end{pmatrix} = \begin{pmatrix} \sum_{n=1}^{N} x_{\mathrm{TR}}(n)q_1(n) \\ \vdots \\ \sum_{n=1}^{N} x_{\mathrm{TR}}(n)q_M(n) \end{pmatrix} \tag{4.26}$$

Equation (4.26) can be solved either by using a numerical algebraic equation solver, or by inverting matrix $\mathbf{Q}$, multiplying the inverse $\mathbf{Q}^{-1}$ on both sides of Equation (4.26) and directly calculating the weights. Note that the singularities of $\mathbf{Q}^{-1}$ must be accounted for in the implementation of the direct solution.

4.3.3 Double Iterative Least Squares Optimization

Consider Equation (4.2) and assume that the piezo disc or the transducer signal and the laser source signals are known. This section describes a procedure to extract $s(n)$ and w_j out of Equation (4.2) in a minimum least squares sense. Note that the recovered source function can not be longer than the length of the original laser source signal, and due to the structure of the algorithm, the length of the number points of useful information in the laser source signal is reduced by the length of the source function (truncated and padded with zeros).

For the extraction of $s(n)$ and w_j the following algorithm is applied:

1. Assume initial weights.

2. Use modified Toeplitz recursion (Section 4.3.1.2) to find $s(n)$.

3. Use Equation (4.26) to calculate weights w_j.

4. Is error small enough? If so, quit.

5. Go back to 2.

This algorithm is referred to as the "double iterative least squares optimization" and was developed and used for similar applications — as in this research — by Michaels et al. [19, 20] and Chang [6]. Note that $s(n)$ and w_j are uniquely obtained only to within a scale factor.

4.4 Frequency Domain Deconvolution Theory

This section presents a frequency domain deconvolution approach under the presence of noise, originally taken for continuous systems by Cooper and McGillem [10] and modified by Michaels [18]. Due to the efficiency of the FFT, frequency domain methods are computationally attractive and also can offer some other advantages over time domain methods.

Consider the time domain case with noise in the signal that is similar to the outline of Toeplitz recursion, but now the noise is explicitly included in the signal.

$$\hat{x}_{\mathrm{TR}}(n) = (x_{\mathrm{LSR}}(n) + N(n)) * s(n) \tag{4.27}$$

where:

$x_{\mathrm{LSR}}(n)$	= known laser signal
$N(n)$	= noise component in the laser signal
$x_{\mathrm{TR}}(n)$	= desired (measured) transducer signal
$\hat{x}_{\mathrm{TR}}(n)$	= recovered transducer signal
$s(n)$	= unknown source function

As written in the last section, the source function is to be determined in a least squares sense, e.g., such that

$$Err = \sum_n (x_{\mathrm{TR}} - \hat{x}_{\mathrm{TR}})^2 \tag{4.28}$$

is minimum. Substituting from Equation (4.27) and rearranging,

$$Err = \sum_n \left[(x_{\mathrm{LSR}}(n) * s(n) - x_{\mathrm{TR}}(n)) + N(n) * s(n)\right]^2 \tag{4.29}$$

can be obtained. Assuming that the laser signal and its noise are uncorrelated, the error can be separated into two components

$$Err = Err_1 + Err_2 \tag{4.30}$$

where

$$Err_1 = \sum_n (x_{\mathrm{LSR}}(n) * s(n) - x_{\mathrm{TR}}(n))^2 \tag{4.31}$$

$$Err_2 = \sum_n (N(n) * s(n))^2 \tag{4.32}$$

Recall that the Fourier Transform $X(\omega)$ of a discrete signal $x(n)$ is defined as

$$X(\omega) = \sum_{n=-\infty}^{\infty} x(n) e^{i\omega n} \tag{4.33}$$

To express the problem in the frequency domain, consider Parseval's theorem

$$\sum_{n=-\infty}^{\infty} |x(n)|^2 = \frac{1}{2\pi} \int_0^{2\pi} X(\omega) X^*(\omega) \mathrm{d}\omega \tag{4.34}$$

The function $|X(\omega)X*(\omega)|^2$ is called the energy density spectrum, since it determines how the energy is distributed in the frequency domain [23]. Necessarily, the energy density spectrum is defined only for finite-energy signals.

One also needs the convolution/multiplication property which states that a convolution in the time domain corresponds to a multiplication in the frequency domain. Thus, Equations (4.31) and (4.32) can be written in the frequency domain as

$$Err_1 = \frac{1}{2\pi} \int_0^{2\pi} (X_{\mathrm{LSR}} S - X_{\mathrm{TR}})(X^*_{\mathrm{LSR}} S^* - X^*_{\mathrm{TR}}) \mathrm{d}\omega \tag{4.35}$$

$$Err_2 = \frac{1}{2\pi} \int_0^{2\pi} N S N^* S^* \mathrm{d}\omega \tag{4.36}$$

Therefore, one can represent the total error written in Equation (4.38).

$$\begin{aligned} Err &= Err_1 + Err_2 \\ &= \frac{1}{2\pi}\int_0^{2\pi} (X_{\mathrm{LSR}} S X_{\mathrm{LSR}}^* S^* - X_{\mathrm{LSR}} S X_{\mathrm{TR}}^* - X_{\mathrm{TR}} X_{\mathrm{LSR}}^* S^* \\ &\qquad + X_{\mathrm{TR}} X_{\mathrm{TR}}^* + N N^* S S^*)\mathrm{d}\omega \end{aligned} \tag{4.37}$$

Define P_N, P_X, and F composed of values and their complex conjugate as

$$\begin{aligned} P_N(\omega) &= N(\omega) N^*(\omega) \\ P_X(\omega) &= X_{\mathrm{LSR}} X_{\mathrm{LSR}}^* \\ F(\omega) F^*(\omega) &= P_N(\omega) + P_X(\omega) \end{aligned} \tag{4.38}$$

Now, use Equations (4.38) to express the overall error

$$Err = \frac{1}{2\pi}\int_0^{2\pi} (X_{\mathrm{TR}} X_{\mathrm{TR}}^* - X_{\mathrm{LSR}} S X_{\mathrm{TR}}^* - X_{\mathrm{TR}} X_{\mathrm{LSR}}^* S^* + F F^* S S^*)\mathrm{d}\omega \tag{4.39}$$

Inside the integral, add and subtract $\frac{1}{FF^*} X_{\mathrm{TR}} X_{\mathrm{TR}}^* X_{\mathrm{LSR}} X_{\mathrm{LSR}}^*$, to obtain the relationship in Equation (4.40).

$$\begin{aligned} Err &= \frac{1}{2\pi}\int_0^{2\pi} (F F^* S S^* - X_{\mathrm{TR}}^* X_{\mathrm{LSR}} S - X_{\mathrm{TR}} X_{\mathrm{LSR}}^* S^* + X_{\mathrm{TR}} X_{\mathrm{TR}}^* \\ &\qquad + \frac{1}{FF^*} X_{\mathrm{TR}} X_{\mathrm{TR}}^* X_{\mathrm{LSR}} X_{\mathrm{LSR}}^* - \frac{1}{FF^*} X_{\mathrm{TR}} X_{\mathrm{TR}}^* X_{\mathrm{LSR}} X_{\mathrm{LSR}}^*)\mathrm{d}\omega \end{aligned} \tag{4.40}$$

Now factor the integrand and obtain

$$\begin{aligned} Err &= \frac{1}{2\pi}\int_0^{2\pi} [(FS - \frac{X_{\mathrm{TR}} X_{\mathrm{LSR}}^*}{F^*})(F^* S^* - \frac{X_{\mathrm{TR}}^* X_{\mathrm{LSR}}}{F}) \\ &\qquad + \frac{X_{\mathrm{TR}} X_{\mathrm{TR}}^* P_N}{P_X + P_N}]\mathrm{d}\omega \end{aligned} \tag{4.41}$$

Note that the last term is a constant since it has no $S(\omega)$ dependence. The two factors in the first term are complex conjugates, e.g., the error reaches its minimum

when either of these two factors is zero. Setting the first one equal to zero, it holds that

$$FS - \frac{X_{\mathrm{TR}} X^*_{\mathrm{LSR}}}{F^*} = 0 \tag{4.42}$$

Solving for $S(\omega)$, obtain

$$S(\omega) = \frac{X_{\mathrm{TR}} X^*_{\mathrm{LSR}}}{P_X(\omega) + P_N(\omega)} \tag{4.43}$$

For the actual implementation, where it is impossible to split the measured signal from its noise component, a practical approach is to estimate the noise power by taking the maximum power of the laser source signal and multiplying it with the estimated signal-to-noise ratio (SNR). This procedure yields Equation (4.44), which can be easily implemented.

$$S(n) = \frac{X_{\mathrm{TR}}(n) X^*_{\mathrm{LSR}}(n)}{|X_{\mathrm{LSR}}(n)|^2 + max|X_{\mathrm{LSR}}(n)|^2 SNR} \tag{4.44}$$

Note that due to the structure of the fast Fourier transform (Butterfly operations), it is advisable to pad the signals with zeros to expand their length to an integral power of two.

4.5 Numerical Examples

This section shows deconvolution results for synthetic source functions and spatial weights. Section 4.5.1 provides a test of the double iterative least squares method. Section 4.5.2 shows some numerical examples for the deconvolution in the frequency domain. These results are useful for understanding the experimental data presented in Chapter 5.

4.5.1 Time Domain

The fact that it is possible to perfectly recover a synthetic source function out of two single signals has already been confirmed in Section 4.3.1.2. Now consider the combination of finding simultaneously the optimal weights w_j and the optimal source time function $s(n)$ with the double iterative least squares algorithm. Therefore consider the following scenario:

A synthetic transducer signal x_{TR} is obtained by evaluating Equation (4.2) — $s(n)$ is the synthetic source function in Figure 4.4(f) (solid line) and w_j are the weights in Figure 4.5(a) (solid line). For the recovery process the following assumptions are made:

- For purposes of illustrating the method, a reduced set of laser source Rayleigh signals consisting of every 5^{th} signal for a total of 21 is used. The remainder are not used.
- For the recovery process the initial weight distribution is rectangular (all weights are equal).
- Three different noise levels (from zero noise to 10 % noise) are assumed for the inversion (see Table 4.1).

Table 4.1: Assumed signal-to-noise ratios for the recovery

	no noise	medium noise	high noise
x_{LSR}	0 %	1 %	10 %

Now, only the synthetic transducer signal and the 21 laser source signals are provided for the double iterative least squares algorithm to recover the source function and the weight distribution, originally taken to calculate the synthetic transducer signal. Both, the source function and the weight-distribution are perfectly recovered if no noise is assumed to be in the signals (original and recovered are the same) which is correct for this synthetic data; a reasonable result is obtained for the assumption of a medium SNR.

If one assumes a high SNR in x_{LSR}, the general shape of the recovered weight distribution (Figure 4.5(a)) is still tolerable, whereas one gets a phase shift in the recovered source function (Figure 4.5(b)) which is obvious only for later times. This effect has to be taken into consideration in later discussions, since the phase information is one crucial feature for physical interpretability. Figure 4.5(c) shows that the algorithm

converges to reasonable values even with the assumption of a high signal-to-noise ratio — the estimated and original signals are almost identical.

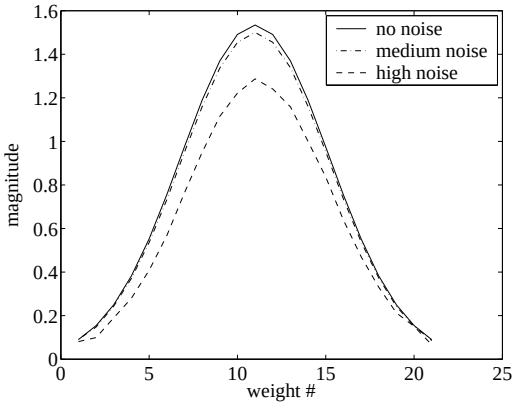

(a) Recovered weight-distributions for different noise levels.

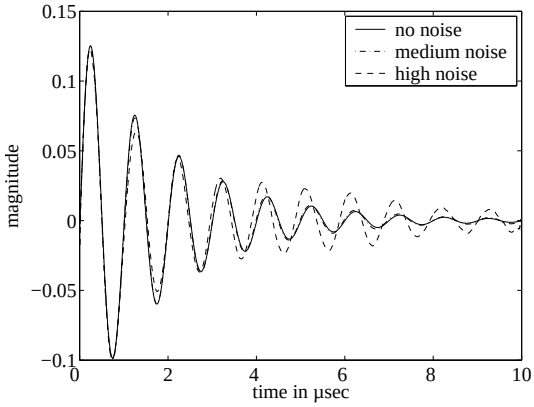

(b) Recovered source functions for different noise levels.

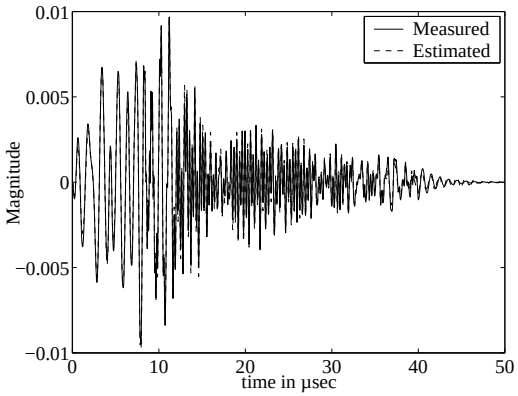

(c) Original and recovered time signals for high SNR.

Figure 4.5: Test for double iterative least squares optimization.

4.5.2 Frequency Domain

As an numerical example for the frequency domain deconvolution, the following scenario is performed. Consider Equations (4.45), (4.46), and (4.47), where $x_{\mathrm{LSR}_{\mathrm{ave}}}$ denotes the average of the reduced laser source Rayleigh set (i.e., every fifth signal), $x_{\mathrm{LSR}_{\mathrm{single}}}$ a single laser source Rayleigh signal, and x_{TR} denotes the transducer source Rayleigh signal. S_2 and S_3 can be considered as source functions, whereas S_1 represents an inverse mapping function. The goal is to calculate the desired source function

S_3 directly from Equation (4.47) and compare this source function to the indirectly recovered source function (from Equation (4.45) and Equation (4.46)) for different noise levels.

$$FFT(x_{\mathrm{LSR_{ave}}})FFT(s_1) = FFT(x_{\mathrm{LSR_{single}}}) \quad (4.45)$$

$$FFT(x_{\mathrm{LSR_{ave}}})FFT(s_2) = FFT(x_{\mathrm{TR}}) \quad (4.46)$$

$$FFT(x_{\mathrm{LSR_{single}}})FFT(s_3) = FFT(x_{\mathrm{TR}}) \quad (4.47)$$

Note that by substituting Equation (4.45) into Equation (4.46), one can see that

$$S_3 = \frac{S_2}{S_1}. \quad (4.48)$$

The presented frequency domain algorithm is applied to recover the source functions and the mapping function to verify Equation (4.48) for three different assumed noise levels.

Recall, that all the signals are filtered to have an effective frequency bandwidth from 500 kHz to 5 MHz. This frequency domain algorithm does an excellent job of recovering the desired source function $s_3(n)$ for the correct assumption of zero noise (Figure 4.6(a)). If the assumed SNR is increased to 1 % in the algorithm, the parts of the spectrum close to the cutoff frequencies of the filter are modeled worse, whereas the effective frequencies are still modeled very well. Increasing the assumed SNR further to 5 % worsens the fitting of the two curves. However, there is still acceptable fitting in the center of the effective frequency bandwidth, e.g., around 2.5 MHz. Note that the signals in this section are padded with zeros to have a total length of 16384 points (integral power of two).

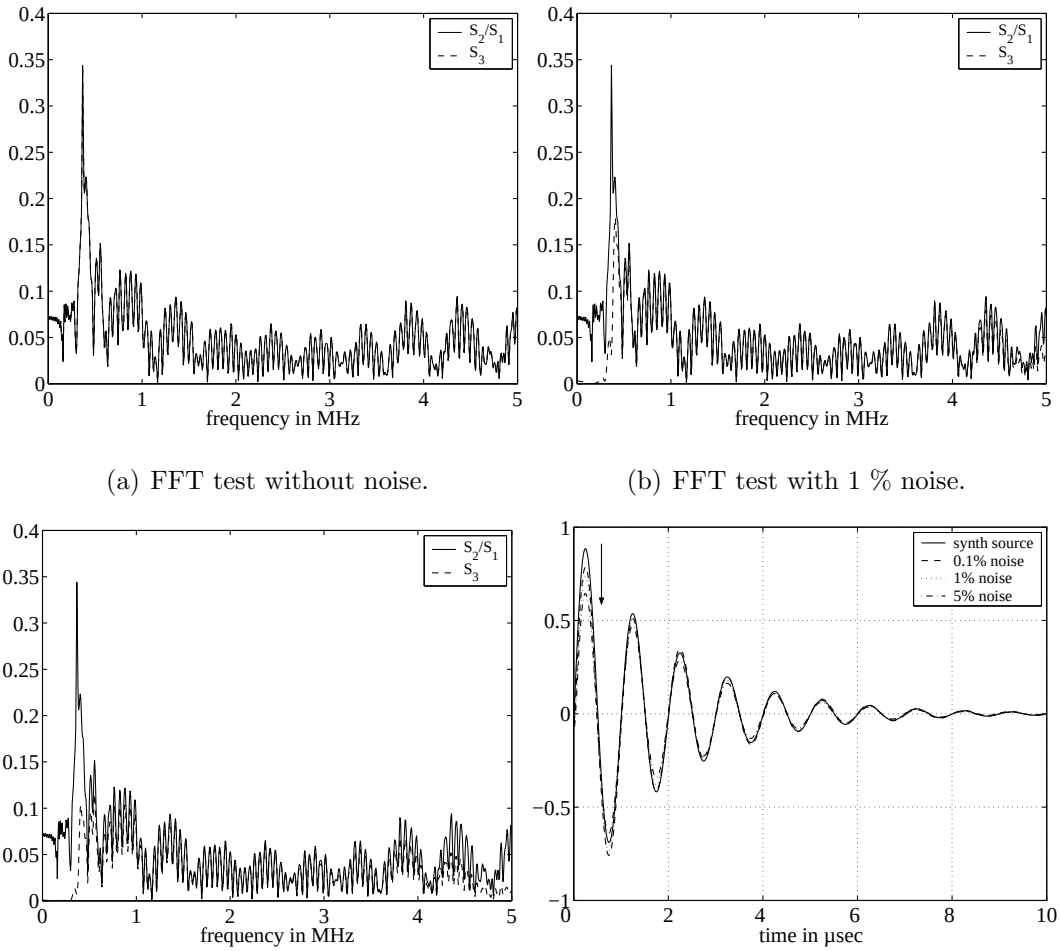

(a) FFT test without noise.

(b) FFT test with 1 % noise.

(c) FFT test with 5 % noise.

(d) Recovered source functions $s_3(n)$.

Figure 4.6: Test of FFT-algorithm with different assumed noise levels.

A second interesting question is: How accurately can one recover the time domain source function? To answer this, convolve a single laser source Rayleigh signal and the synthetic source function of Figure 4.2(b), and perform a deconvolution in the frequency domain. Then take the inverse Fast Fourier Transform of the recovered source function and compare the result with the initial synthetic source function. This test is also made for assumptions of different levels of noise. The results are depicted in Figure 4.6(d), where the presented source function $s_3(n)$ consists of the first 1000 points. Note, that there is no phase shift in the recovered source functions, but by increasing the assumed SNR in the algorithm, the amplitude values have a downward tendency, thus resulting in an amplitude offset.

4.6 Discussion

The last two sections show that in general, one can expect very good deconvolution results for both, the time -and the frequency domain algorithms. However, each method has its advantages and disadvantages as soon as one considers superimposed noise in the signals. Recovered source functions with the time domain method are slightly phase shifted, particularly for later times, compared to the original source function. The ones recovered with the frequency domain algorithm exhibit an amplitude offset. Moreover, if one uses the frequency domain algorithm and performs (Inverse-) Discrete Fourier Transforms, the results will be circularly shifted. As a matter of fact, the main advantage of this method is the arbitrary length of the recovered source function as well as the possibility to interpret causality issues. The advantage of the time domain deconvolution is that one does not have to deal with the uncertainties of FFT and inverse FFT (i.e. circular shift and padding of zeros). As seen in the numerical examples, assumed noise levels can influence the recovered source functions. This is because deconvolution is an inverse process, and like many inversion methods it is sensitive to the effects of even small amounts of noise in the data.

CHAPTER 5

Experimental Results

5.1 Time Domain

5.1.1 Single Laser Source

First consider the laser source data set and determine if it is possible to develop an accurate source function for either (or both) the piezoelectric disc or commercial transducer source with a single laser source signal. The mean square error between the estimated and measured piezo disc or transducer signals (Equation (4.13)) is calculated using each laser source measurement as the impulse response — this helps determine the most appropriate laser source signal (if any) to use out of this multiple set of measurements. Figure 5.1 shows the mean square error as a function of measurement location for the Lamb wave measurements (top) and the Rayleigh wave measurements (bottom) for both the piezo disc and the transducer.

Consider Figures 5.1(a) and 5.1(b). It is clear from these figures that both the piezo disc and the transducer from the Lamb wave measurements are best modeled by taking the laser source measurement at the front edge of the source — the shortest source receiver propagation distance. Note that the lowest measurement location corresponds to the longest propagation distance and vice versa. In contrast, Figures 5.1(c) and 5.1(d) show that all the measurement points after ♯ 15 are effective in modeling the piezo disc or commercial transducer sources — the signals are not linearly independent. The following observations are possible:

- The results are very dependent on the wave type (Lamb or Rayleigh)
- Rayleigh waves are non-dispersive, so they are essentially just shifted versions

of themselves; therefore it makes most sense to select a measurement distance close to the propagation distance that corresponds to the center of the source.

Table 5.1 presents the laser measurement numbers chosen for the subsequent discussions.

Table 5.1: Chosen measurement numbers for single laser

Measurement Set	Location ♯	Source/Receiver Distance
piezo source Lamb	90	42.1 mm
transducer source Lamb	91	42 mm
piezo source Rayleigh	60	45.1 mm
transducer source Rayleigh	60	45.1 mm

Note that all the arrival times of the signals are adjusted to compensate for fixed instrumentation delays so that the arrival of the piezo disc or transducer signal is slightly earlier than the one of the single laser signals in the center of the measurement set (by an amount equal to the propagation time from center to front edge of piezo disc or transducer). This is because of the spatial extent of the mechanical source. Note also that the entire set of data is bandpass filtered prior to processing with a Butterworth low-pass filter (cutoff frequency 5 MHz) and a Butterworth high-pass filter (cutoff frequency 500 kHz). Using these preprocessed signals, the recovered source functions are shown in Figure 5.2. A first obvious feature in all four source functions, particularly evident in the Rayleigh data, is the two very pronounced peaks. The ratio between peak amplitude and the rest of the signal in the source functions in Figure 5.2(a) and Figure 5.2(b) (Lamb data) is about half of the ratio for the signals in Figure 5.2(c) or Figure 5.2(d) (Rayleigh data). Inspection of the less complicated source functions of the Rayleigh signals shows that the second peak is approximately a delayed version of the first peak. A propagation distance between the peaks is calculated from the Rayleigh wave speed and the time between the two peaks. The outcomes of this calculation are shown in Table 5.2, where a Rayleigh wave speed of 3100 $\frac{m}{s}$ is assumed. One can immediately see that the two major peaks correspond to the effective width (diameter) of each of the piezoelectric sources. Note that there is a second set of two peaks in the Rayleigh measurements that are delayed

from the first two peaks; their time difference also corresponds to the source diameter.

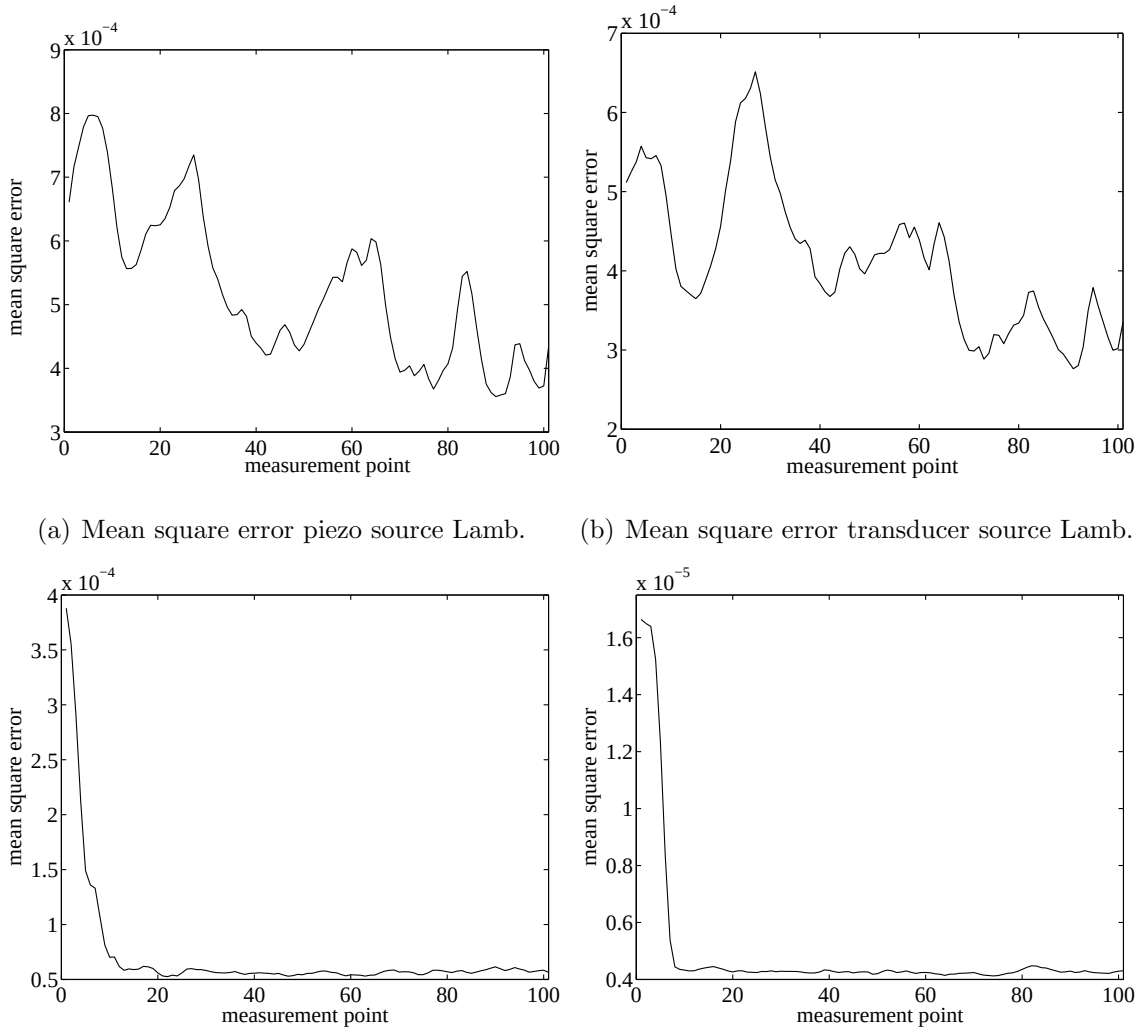

(a) Mean square error piezo source Lamb.

(b) Mean square error transducer source Lamb.

(c) Mean square error piezo source Rayleigh.

(d) Mean square error transducer source Rayleigh.

Figure 5.1: Mean square errors.

Table 5.2: Calculated distances corresponding to the first two main peaks

	measured time pk-pk	calculated distance	effective diameter
piezo disc	1.6 μsec	5.177 mm	5.2 mm
transducer	1.93 μsec	5.983 mm	6 mm

Since it is expected that the source functions describe or model the behavior of the

mechanical source, it has to be asked why the source functions for the Lamb data in Figures 5.2(a) and 5.2(b) are non-zero before the first large peak arrives. A delay would not be a problem, since it would just represent the time before the piezo disc or commercial transducer is stimulated, and in this time there would obviously be no movement. But if the magnitudes of the source function before the first peak are non-zero values, the source function exhibits anti-causal behavior and one must question its usefulness as a physical interpretation of the source. In contrast, taking a look at the source functions of the Rayleigh signals, reasonable results are obtained. Both source functions start out at zero, gradually increase their amplitude, which could correspond to the contraction or expansion of the piezoelectric source, until it reaches a maximum, and expands or contracts afterwards to form the peak in the opposite direction. This is the typical feature of a dipole.

Note that if the model were perfect, the source functions in Figures 5.2(a) and 5.2(c) should be the same, and those of 5.2(b) and 5.2(d) should be the same, as is confirmed by the following argument. Suppose all external effects on the "perfect" signal from an unbounded — such as reflections, temperature effects and internal effects in the measurement unit — are represented by $\Upsilon(t)$. Since the measurements are performed by the same instrumentation and at the same location on the specimen, $\Upsilon(t)$ is the same for the piezo disc, commercial transducer, and laser source measurements.

Now, define $G(t)$ to be the true impulse response of the unbounded medium (either the plate or the half space). With the defined $G(t)$ and $\Upsilon(t)$ the measured laser and transducer signals can be expressed as written in Equations (5.2).

$$\begin{aligned} x_{\mathrm{LSR}}(t) &= G(t) * \Upsilon(t) \\ x_{\mathrm{TR}}(t) &= G(t) * \Upsilon(t) * s(t) \end{aligned} \tag{5.1}$$

Note that $s(t)$ denotes the transducer source function. Rewriting and substituting Equations (5.2), Equation (5.3)is obtained, and it can be seen that the external effects

$\Upsilon(t)$ simply cancel each other out.

$$\begin{aligned} x_{\mathrm{TR}}(t) * \Upsilon(t) &= s(t) * x_{\mathrm{LSR}}(t) * \Upsilon(t) \\ x_{\mathrm{TR}}(t) &= s(t) * x_{\mathrm{LSR}}(t) \end{aligned} \tag{5.2}$$

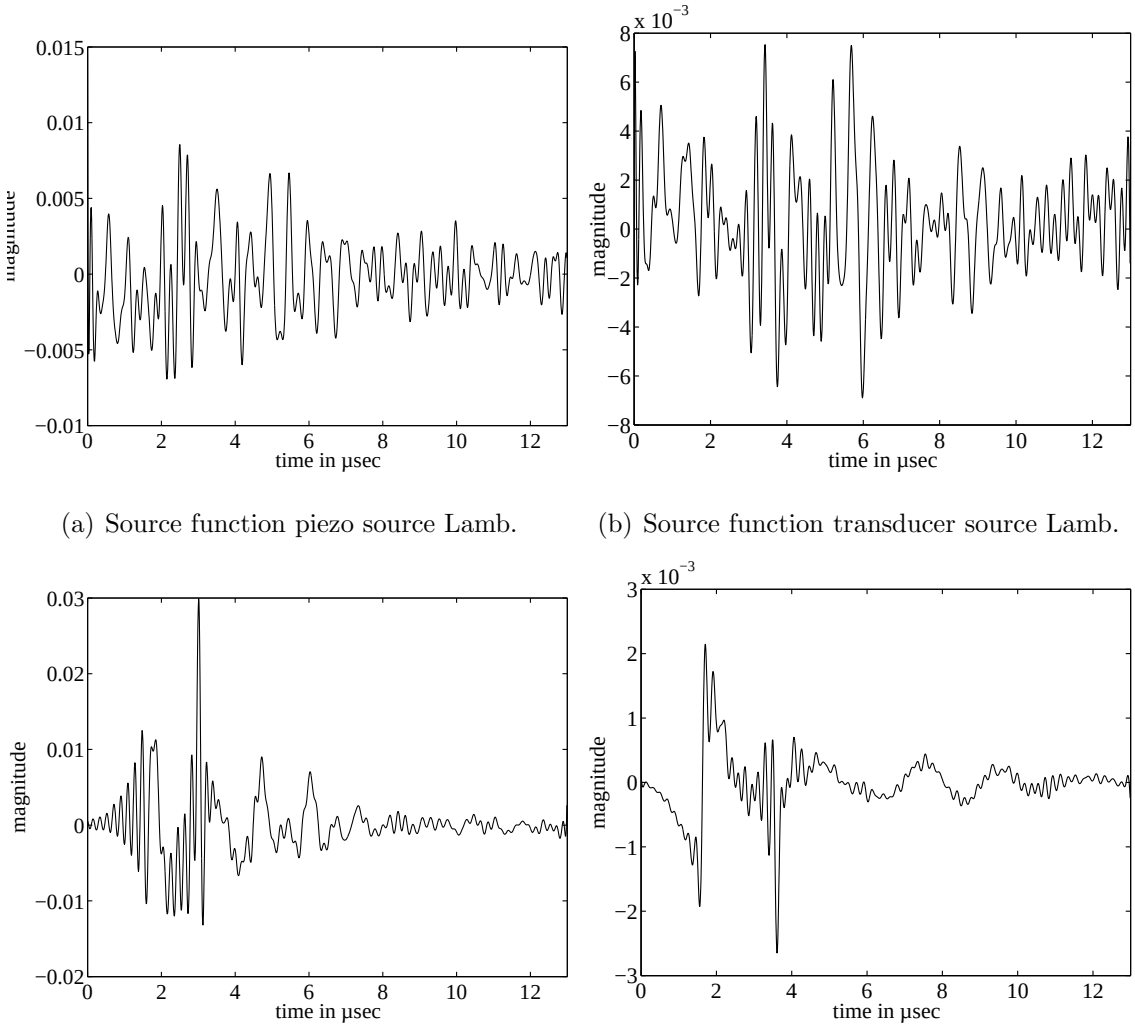

(a) Source function piezo source Lamb.

(b) Source function transducer source Lamb.

(c) Source function piezo source Rayleigh.

(d) Source function transducer source Rayleigh.

Figure 5.2: Source functions.

Hence, the fact that $G(t)$ and $\Upsilon(t)$ for the half space are different from $G(t)$ and $\Upsilon(t)$ for the plate does not affect the process of recovering the source function. But, since the source functions for the Rayleigh and Lamb measurements are significantly

different, an expansion of the convolution model of Equation (4.8) is necessary. Now, the spatial extent of the piezo disc or commercial transducer, as well as its temporal effects, must be taken into account.

5.1.2 Averaged Laser Source

5.1.2.1 Forward Modeling of the Averaged Laser Source

Section 4.2 already shows that the effects of averaging the laser signals should be taken into account in order to improve the model of the commercial transducer or the piezo disc. Now, determine how "well" the piezo disc and commercial transducer sources can be modeled by applying certain weight distributions to a summation of single laser measurements. Note that all the results presented in this section are based upon the plate data. Since the major interest of this research is in the effects of the source on the dispersion curves, only the first arrivals of the Lamb waves is shown, i.e., the time axis is truncated to cut off all edge reflections. Three different axially symmetric weight distributions over the circular source area are considered: a piston distribution, a Gaussian shaped distribution and an inverted Gaussian distribution.

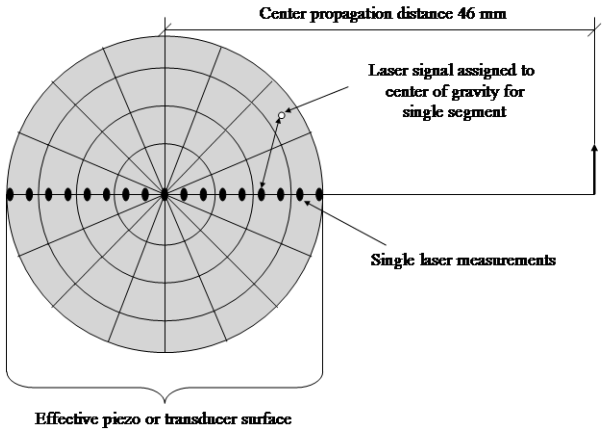

Figure 5.3: Simplified scheme of how single laser signals are assigned to the segments on the effective transducer or piezo surface.

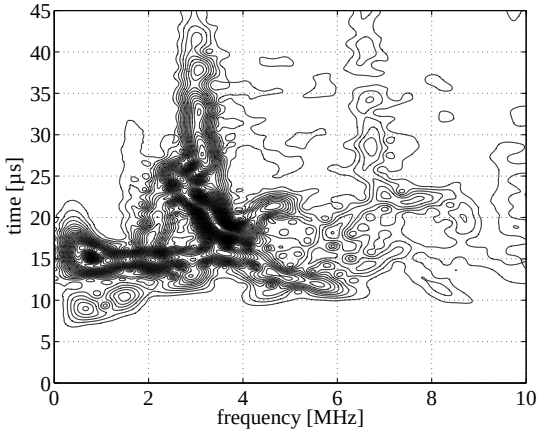

(a) Piston model.

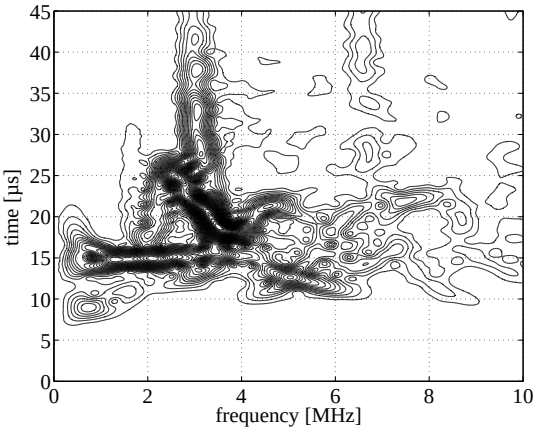

(b) Gaussian model.

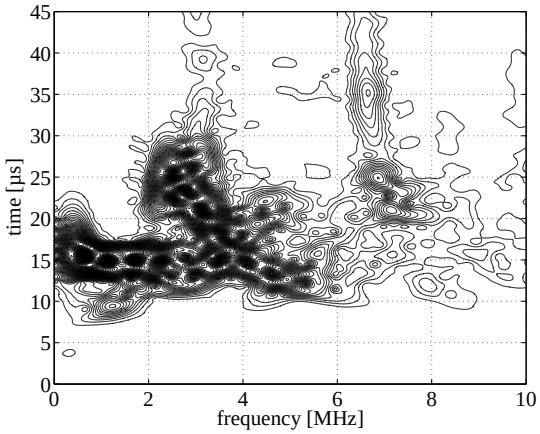

(c) Inverted Gaussian model.

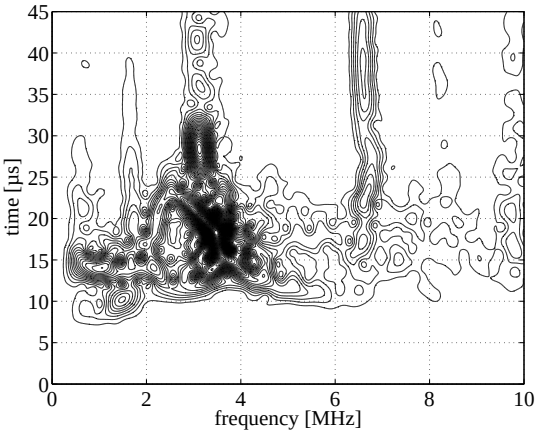

(d) Commercial transducer.

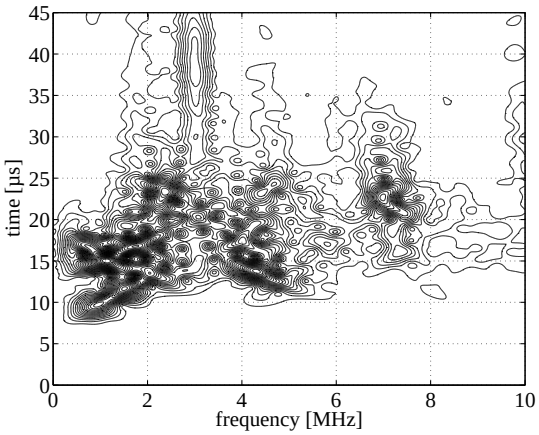

(e) Piezoelectric disc.

Figure 5.4: Comparison of different weight distributions for averaging laser signals.

The resulting un-reassigned STFTs of the three modeled laser signals will then be compared with the un-reassigned STFTs of the measured commercial transducer

and piezo disc data.

The piezo disc and transducer are modeled according to the general schematic shown in Figure 5.3. The effective surface of the mechanical source is divided into ten rings of equal area, where each of these rings is further divided into 64 curved elements of equal area. Each element's area is proportional to the weight of the corresponding "laser source Lamb"-signal. This signal is found by calculating the propagation distance from the center of the elements and assigning it to the closest available distance in the measured laser set. The weights are further modified as needed to generate the desired profile (i.e., piston, Gaussian, or inverted Gaussian).

All STFTs for these synthetic signals are shown in Figure 5.4 along with the actual piezo disc and transducer STFTs. Comparing Figures 5.4(a) and 5.4(b), it can be seen that the piston and the Gaussian profiles result in similar dispersion curves. They both have a "hot spot" at 3.25 MHz and 20 μs. This "hot spot" seems to be characteristic of the commercial transducer shown in Figure 5.4(d). Note that this highly concentrated energy density does not appear in the dispersion curves for a single laser signal. Furthermore, note that the piston profile shows higher energy density between 0.5 MHz and 1 MHz at 17 μs as compared to the Gaussian profile. This fact indicates that using a Gaussian profile instead of a piston profile improves the model, since the energy density of the commercial transducer is low below frequencies of 3 MHz. Figure 5.4(c) shows the result obtained using the inverted Gaussian window, which results in broader and more "broken up" dispersion curves (note the dark spots). The energy density for this case is high for frequencies below 3 MHz, but relatively low for higher frequencies. This phenomenon also appears for the dispersion curves of the piezo disc. To justify the choice of an inverted Gaussian weight distribution as a model for the piezo disc, consider the fact that the piezoelectric disc is glued to the plate. The piezo disc is excited in the center and the mechanical force then propagates to the outermost regions of the disc. Since the piezo disc is glued, the excitation impulse is introduced into the specimen surface at these outermost regions. If the mechanical source is not glued, but is instead oil coupled as for the commercial

transducer, this energy will not be transmitted into the plate, i.e., this mechanical energy simply propagates back and forth in the transducer and dissipates. This conclusion is corroborated by the finite element model results of Duquenne et al. [11], for calculations of the normal stress of a bonded rectangular piezoelectric element.

5.1.2.2 Source Inversion for Averaged Laser Source

Now take a closer look at the error plots of Figure 5.1. As mentioned in Section 5.1.1, the optimal single laser signal for Lamb waves to model the mechanical source are the ones which have the closest source to receiver distance. In contrast, the best signal to model the Rayleigh signals are the ones in the center. Taking this knowledge into consideration, the piezo disc or commercial transducer is modeled with $\frac{h}{0.1 \text{ mm}}$ laser source signals centered at signal m for the Rayleigh waves, and $\frac{h}{0.1 \text{ mm}}$ signals from $l - \frac{h}{0.1 \text{ mm}}$ through l for the Lamb waves, where h is the effective surface diameter of the mechanical source, m the optimal signal number for the Rayleigh wave in Table 5.1 and l the optimal signal number for the Lamb waves in Table 5.1. These relationships are used to calculate the effective measurement numbers presented in Figure 5.3.

Table 5.3: Chosen measurement numbers for averaged laser

Measurement Set	Range for Location ♯	Range for Source/Receiver Distances
piezo source Lamb	38-90	47.3 mm-42.1 mm
transducer source Lamb	31-91	48 mm-42 mm
piezo source Rayleigh	34-86	47.8 mm-42.5 mm
transducer source Rayleigh	30-90	48 mm-42 mm

A large number of experiments confirms that all scenarios performed with the algorithm described in Section 4.3.3 converge after 50 iterations. Now, the double iterative least squares method is used to simultaneously recover the weight distributions in Figure 5.7 and the source functions depicted in Figure 5.8. As mentioned in the last section, the use of ring signals is crucial to obtain physically meaningful

results. However, the double iterative least squares optimization is implemented to optimize the weights of a line source (line signal consists of the laser set) in contrast to the area source (piezo disc or transducer). To make this line signal applicable to the algorithm, only every fourth laser source measurement is taken for the commercial transducer with an effective diameter of 6 mm (spatial separation distance of 0.4 mm, i.e., 16 weights) and every third laser source measurement for the piezo disc with an effective diameter of 5.2 mm (spatial separation distance of 0.3 mm, i.e., 18 weights). To further support the idea of using reduced line signals, it is important to note the fact that the equations do not "know" the physics of the particular sources. Hence, the pure math will just develop the optimal solution, but not necessarily the physically most meaningful solution, for the given amount of information — which is the number of single laser source signals to model the mechanical source. Hence, to avoid obtaining physically meaningless results, a reduction of this information to a degree where the math fits or models the physics is necessary. With these initial considerations, the distribution of the weights (Figure 5.7) for the four considered cases is discussed.

First consider the weight distributions for the plate measurements. A bias to the front edge of the mechanical source is visible. Note that the highest measurement location corresponds to the shortest propagation distance. This location of the maximum weight correlates to the minimum least square error (mse) of the single laser source in Figure 5.1. The correlation to the mse is meaningful in the sense that the single signal that models the piezo disc or transducer the best, should have the biggest weight among the set of weights. Since there is a descent of the mse in Figures 5.1(a) and 5.1(b), it is understandable that the weights are shaped with an envelope that roughly corresponds to the inverse of the descent.

For the physical background or meaning of weight distributions, a careful look at the source functions in Figures 5.8(a) and 5.8(b) has to be taken. Both source functions contain a significant 3.2 MHz component, as can be seen from their spectra (not shown). This frequency corresponds to the reverberations in the plate; i.e., the 2-way

travel time of the L-wave through the plate thickness. At this point, one could argue that it is not possible that the source function contains reverberations since they would be canceled out as shown in Equation (5.3). But this is not the whole truth for the Lamb wave case. To explain this fact, an additional $\breve{\Upsilon}(t)$ is defined — it models how the piezo disc or the transducer modifies the impulse response. The mechanical source which is mounted to the surface of the plate changes the boundary conditions in the mounting area, and therefore the properties of the reflections. This scenario is depicted in Figure 5.5.

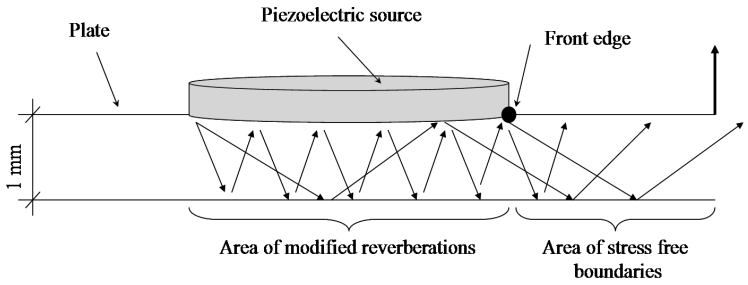

Figure 5.5: Change of boundary condition due to mounting of mechanical source.

However, using the laser source, the boundary condition does not change. Hence, the modified deconvolution problem can be written as follows:

$$x_{\mathrm{TR}}(t) = s(t) * x_{\mathrm{LSR}}(t) * \breve{\Upsilon}(t)$$

It is obvious that $\breve{\Upsilon}(t)$ remains in the deconvolution problem and thus appears combined with the recovered source function. Thus, the closer the laser signal is to the front edge of the piezo disc or transducer, the less the modified reverberations affect the signal, i.e., it is less distorted and therefore closer to an undistorted laser source signal.

Now, the weight distributions of the Rayleigh signals in Figure 5.7(c) and 5.7(d) have to be observed. There is a Gaussian like shape in both plots, which is not unexpected. By taking a closer look at the magnitudes of the two weight distributions, one notes that the predictions and observations made in the forward modeling of the mechanical sources are confirmed. The weight distribution in Figure 5.7(c) corresponds to an

inverted Gaussian (i.e., maximum amplitudes are at either end), whereas the weights in Figure 5.7(d) represent a Gaussian shaped profile, multiplied by -1 (i.e., maximum negative amplitude is in the center).

For these observations two points are crucial. The first point is that the weights for the glued disc still tend to be biased to the front edge of the disc (shortest propagation distance). This could be due to coupling effects, inaccuracies in the bonding process, physics of the disc itself or oscillations in the disc. These effects are qualitatively illustrated in Figure 5.6. The second point involves an understanding of the negative weights for the commercial transducer. Recall that the double iterative algorithm does not yield unique scale factors for w_j and $s(n)$ since they are present as a product in Equation (4.2). The source function has a negative sign and the weights also have a negative sign, which makes sense in combination.

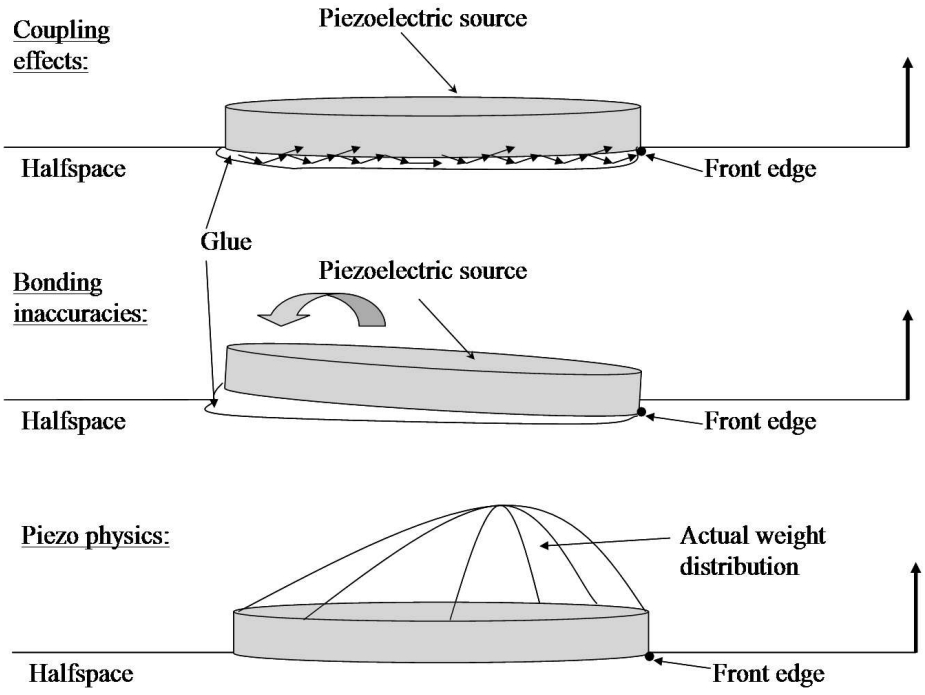

Figure 5.6: Effects of piezo disc on half space.

Now, why does the extraction of meaningful weights seem to work for the Rayleigh waves, but not for the Lamb waves? There are no reverberations affecting our 13 μsec

long Rayleigh source functions, since the half space is too high; that is, the first reflection from the bottom arrives after about 33 μsec. Figures 5.8(c) and 5.8(d) show the corresponding Rayleigh source functions.

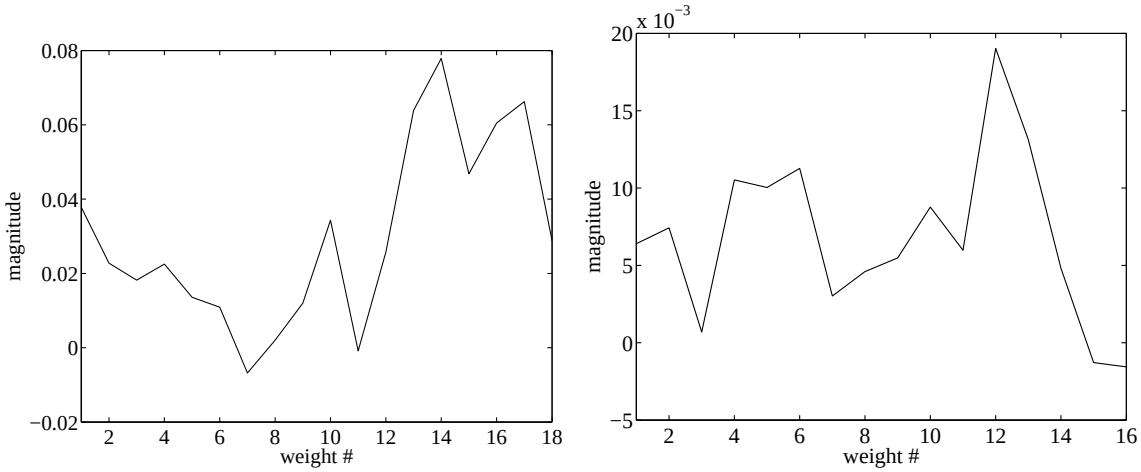

(a) Weights for averaged piezo source Lamb.

(b) Weights for averaged transducer source Lamb.

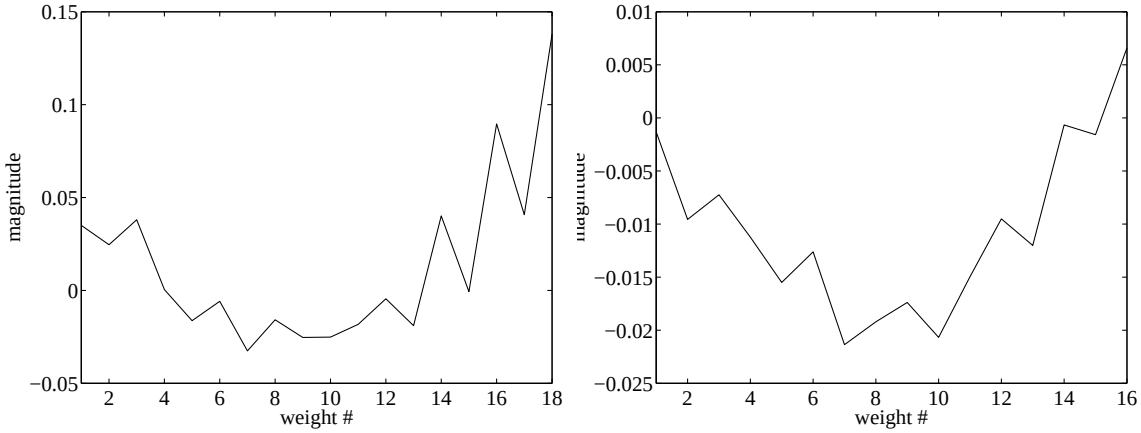

(c) Weights for averaged piezo source Rayleigh.

(d) Weights for averaged transducer source Rayleigh.

Figure 5.7: Weight distributions.

Comparing these source functions with the ones from the single laser source signal in Figure 5.2, it can be noted that the second peak at 3-3.5 μsec is much lower in amplitude if the laser signals are averaged. This is also generally the case for the source functions recovered from the Lamb wave measurements.

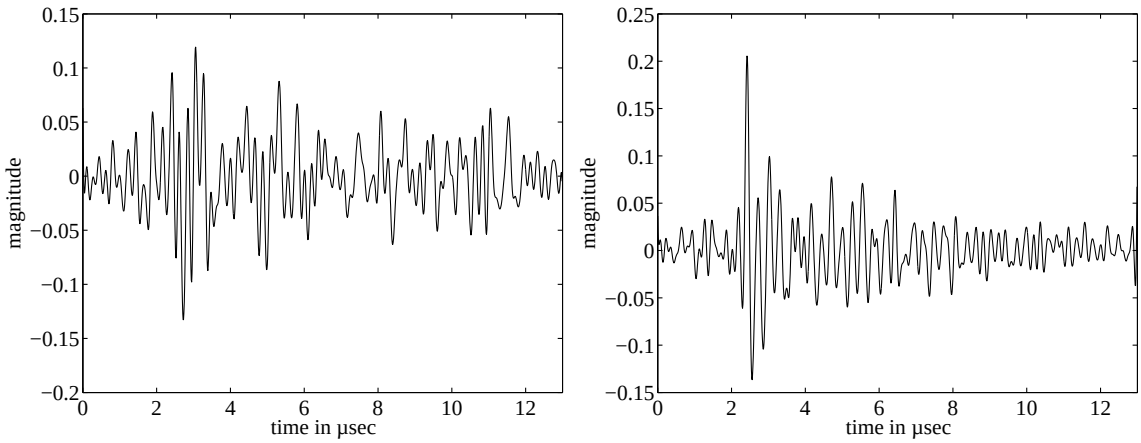

(a) Source function for averaged piezo source Lamb.

(b) Source function for averaged transducer source Lamb.

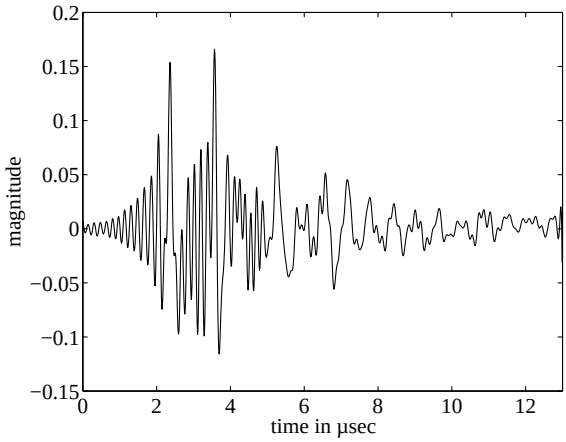

(c) Source function for averaged piezo source Rayleigh.

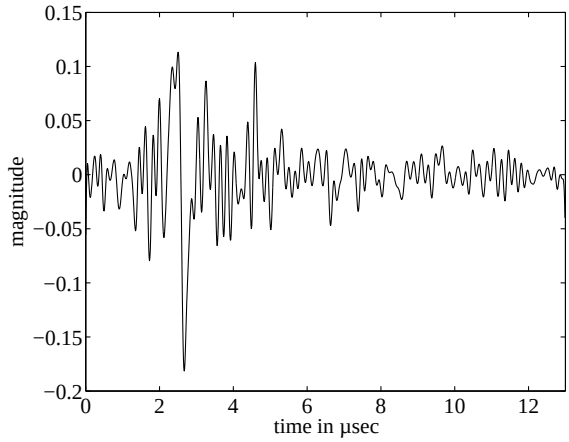

(d) Source function for averaged transducer source Rayleigh.

Figure 5.8: Source functions for averaged signals.

5.2 Frequency Domain

This section approaches the source function issue from a less descriptive but more mathematical point of view. Note that up to this point, the source function was always calculated so that when convolved with a laser signal, the measured piezo disc source signal was obtained. This way was chosen for interpretation purposes; i.e., to understand the physics of the mechanical source. Now considered is a so-called "black box" approach in which frequency domain methods are used to calculate an

inverse function that when multiplied (in the frequency domain) with a piezo disc or transducer signal recovers the laser signal. This inverse function does not have a direct physical interpretation.

Figure 5.9 shows the results of the following scenarios: A 10000 point (100 μs) "laser source Lamb"-signal (Figure 5.9(a)) and a 10000 point "piezo source Lamb"-signal (Figure 5.9(b)) are padded with zeros to have a length of the next higher integral power of two (16384). Then a deconvolution is performed to calculate a 16384 point inverse function. A presence of 0.5 % SNR is assumed for the algorithm. To test the approach, the inverse function is multiplied with the piezo disc signal (without considering noise). The result is inverse Fourier transformed and a spectrogram is calculated and depicted in Figure 5.9(c). It seems that the recovered "laser source Lamb"-signal (Figure 5.9(c)) is modeled essentially perfectly up to 30 μsec, but for later times, slight variations in the energy density of the reflections are visible. In fact, these variations are over the entire length of the recovered signal, but are not visible due to the high energy density of the early arrivals. These variations occur because of the noise.

Now, a more complex case will be evaluated. An inverse function is calculated for only the first 3000 points of the "laser source Lamb" -and the "piezo source Lamb"-signals. Recovery of the laser signal is still performed with the 10000 points "piezo source Lamb"-signal by multiplying the piezo signal by the inverse function in the frequency domain. Figure 5.9(d) shows the reassigned dispersion curves of the recovered laser signal. Despite some 0.5 MHz noise before the first arrival, the first 3000 points are modeled fairly well by the algorithm; however, the actual range of interest is between 3000 and 10000 points. If there were perfect modeling of the laser signal in this range, it would mean that the inverse function is able to remove the entire effect of the mechanical source. Obviously, this is not the case; besides the noise, Figure 5.9(d) shows the first reflection with a very high energy density compared to the laser signal — more similar to the piezo disc signal, but not as defined. For even later components, there is no interpretable pattern visible. Therefore it can be concluded that by simply

applying a source function, which contains only information of about the first third of the entire signal, to the piezo disc signal a laser-like dispersion relationship of a plate cannot be reliably recovered. This methodology my still be effective for recovering changes in dispersion curves due to damage; this application is not considered here.

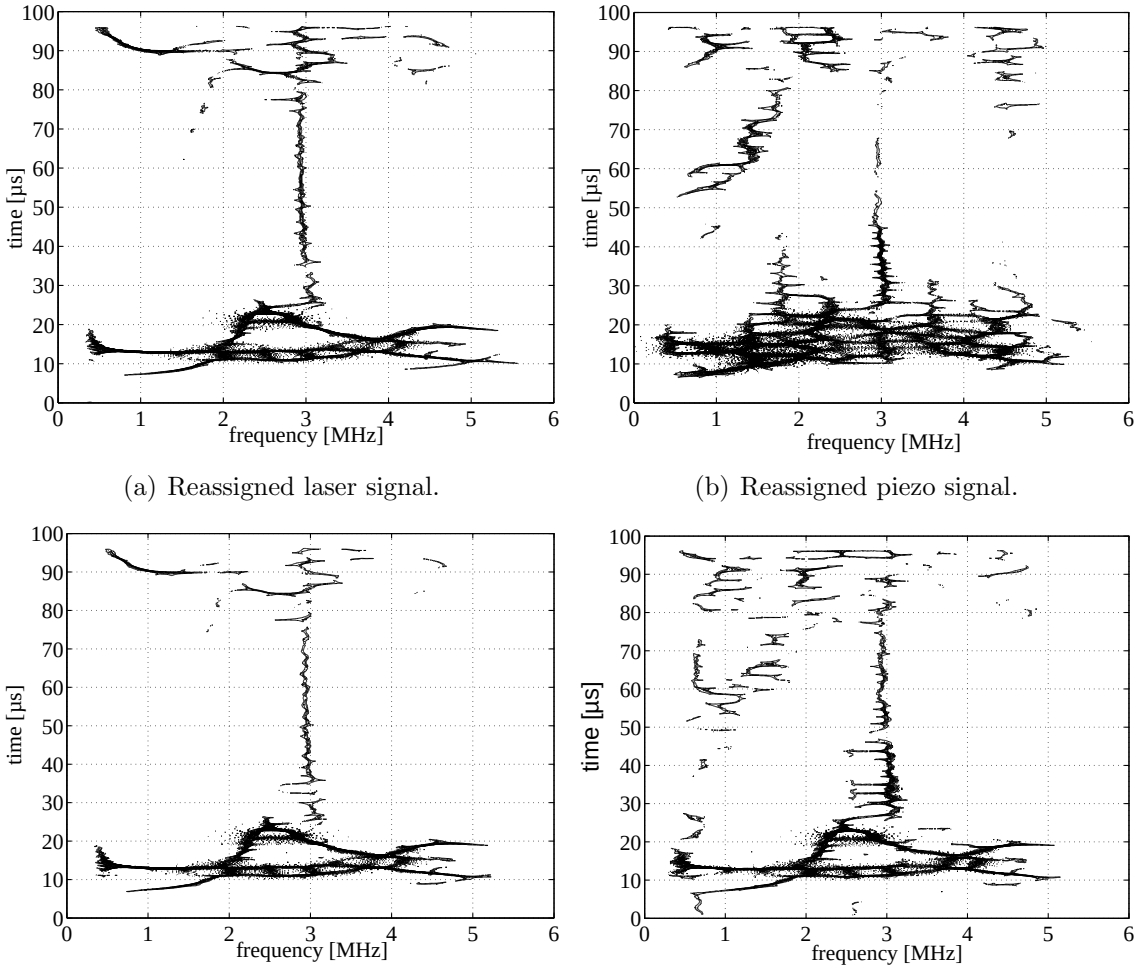

(a) Reassigned laser signal.

(b) Reassigned piezo signal.

(c) Reassigned recovered laser signal 10000 pts source info.

(d) Reassigned recovered laser signal 3000 pts source info.

Figure 5.9: Frequency domain inversion of piezo source signal.

CHAPTER 6

Analysis of Results and Further Considerations

6.1 Time Domain Considerations

Recall that the source function is a representation of the modified physics and the geometry of the piezo disc or the transducer. These modifications are due to the following features:

- spatial extent of the mechanical source
- temporal effects, i.e., ringing of the source and instrumentation
- effects of the coupling or the glue
- modified reverberations due to change of the boundary condition

As seen in previous sections, it is very difficult to precisely extract all these features out of the source function with the current state of understanding of the source function approach in the time domain. To improve this understanding of the source function itself, a more general look at the mathematical meaning of the source function is necessary.

First note that many mathematical models of the piezo disc or transducer signal are possible, e.g.,

$$x_{\mathrm{TR}}(t) = x_{\mathrm{LSR}}(t) * s(t) \tag{6.1}$$

$$x_{\mathrm{TR}}(t) = s(t) * \underbrace{\sum w_j x^j_{\mathrm{LSR}}(t)}_{x_{\mathrm{LSR_{ave}}}(t)}. \tag{6.2}$$

All of these models incorporate a source time function which captures certain properties of the piezo disc or the transducer, e.g., in *s(t)* of Equation (6.1) the spatial extent. Note that this spatial extent is not modeled in the source time function of Equation (6.2), since it is already included in the weighted Green's functions of the averaged laser source signal $x_{\mathrm{LSR}_{\mathrm{ave}}}(t)$. Ideally (in a physical sense) the source time function should only capture the temporal behavior of the source (including instrumentation) and not any effects of the structure, as for instance, coupling.

The better the model of all of the non-temporal aspects of the system, the more accurate the recovered source time function will be. Modifying the model further, so that temporal aspects are also captured, the function $s(t)$ will converge to a delta impulse. In this case, $s(t)$ cannot be considered as a source time function any more.

Now, the idea of using the characteristics of the source time function to evaluate a model is proposed; that is, the source time function is used as a metric of the model. These characteristics are for example:

- causality
- compact support
- impulse-like nature

These characteristics were shown for the spatial extent of the piezo disc or the transducer — originally (modeling with only one single laser signal (Figure 5.2)) two distinct peaks are visible in the source function which indicated that a spatial model needed to be implemented to explain the behavior (Figure 5.8). Note that even though it is a big advantage to be able to interpret some of the characteristics of the source function, it is also possible that other features may overlap or cancel each other out. This could be one more reason, why the source functions recovered from the Rayleigh data differ from the ones obtained from the Lamb data.

Finally note that the source time functions in Figures 5.2(a) and 5.2(b) show that the model is bad, since there is a large non-causal part before the actual peaks and they

do not show any impulse like features. If these source time functions are compared to the source time functions in Figures 5.8(a) and 5.8(a), it can be concluded that the model is much better, since the anti-causal part almost disappears and the source time functions look much more impulse-like, especially the plot in Figure 5.8(a).

6.2 Frequency Domain Considerations

6.2.1 Recovery of Reflections

Recall that Section 5.2 tried to determine an inverse function in the frequency domain to recover the dispersion relationship of a laser signal from a signal obtained with piezo disc or transducer excitation. This worked well for the case where the original and recovered signal had identical length, but failed for the case where the recovered signal and its reflections were predicted (in a sense to recover a reflection). This section shows why this prediction failed by inspecting the less complex and non-dispersive Rayleigh wave data.

Figure 6.1(a) shows two Rayleigh waveforms in the time domain truncated after the first reflection. The solid line waveform is obtained from laser excitation and the dashed line waveform is obtained from transducer excitation. The region of interest is the first reflection after about 34 μsec. This first reflection is very pronounced for the transducer excitation whereas it almost disappears for the laser excitation. To be able to compare the reflection and the first arrivals of the two waveforms the ratios of the amplitudes of first arrival and reflection are considered. Since the ratio for the laser waveform differs from that of the transducer waveform, it will be impossible to reconstruct the laser signal out of the transducer measurement, as shown in the appendix. If the inverse function were to be applied to the transducer signal, a very pronounced reflection would appear in the recovered laser signal — but this reflection obviously is far smaller for the measured laser waveform.

A second observation can be made by looking at the shape of the reflection. This

shape changes for the signal obtained by transducer excitation. The first arrival shows two separated peaks, whereas the reflection appears to be only one peak. This could be due to destructive interference at the receiver position. The fact that the shape of the reflection changes is one further reason why the inverse function may not appropriately recover the laser signal. If the reflected laser source signal does not exhibit the same type of shape change as the transducer signal, the recovery of the laser source signal will be poor. Figure 6.1(b) depicts the original and the recovered laser signal (first arrival). As shown, only a single large peak is recovered.

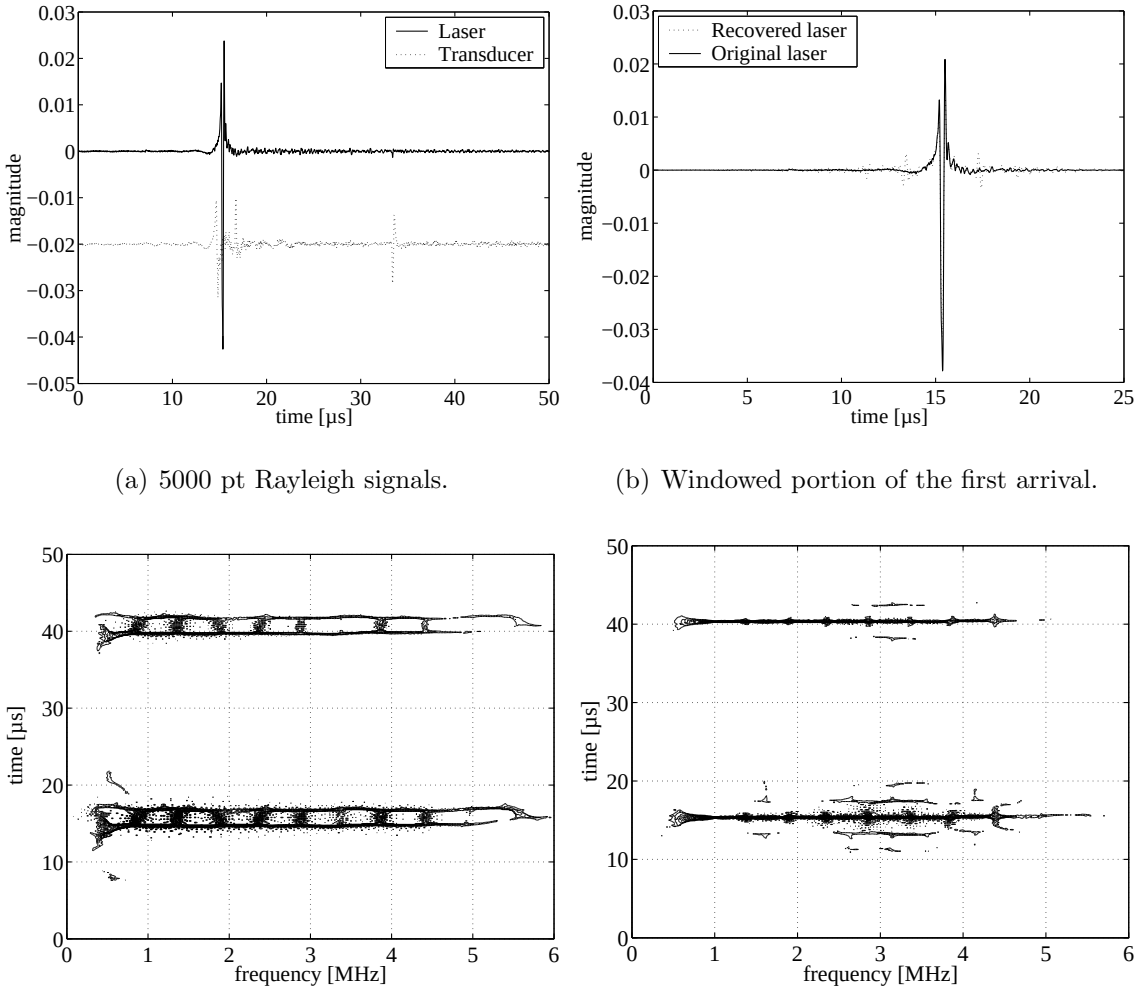

(a) 5000 pt Rayleigh signals.

(b) Windowed portion of the first arrival.

(c) Reassigned original Rayleigh transducer signal.

(d) Reassigned recovered Rayleigh laser signal.

Figure 6.1: Black-box approach remarks.

If the shape of the reflection changes, for example, such that the reflection consists

of two peaks instead of a damped version of the first single peak (or vice versa), the inverse function will still "try" to recover this one peak but will actually be applied to the two peaks and will thus recover the reflection incorrectly. This means that the shape of the reflection (compared to the first original arrival) has to be consistent between the laser source signal and the transducer signal.

To show the expected recovery of the laser signal from the transducer signal, the first reflection of the laser signal is modeled in the following manner. The transducer signal is truncated after the first arrival, e.g., after 2500 points. The truncated version of the signal is windowed with a Kaiser window. After that, a damped copy (half of the amplitude of the original arrival) is appended to the first original arrival. This is a representation of the actual first arrival and its perfect or ideal reflection. Figure 6.1(c) shows the reassigned spectrogram of the this composed signal. Now, the inverse function can be calculated from the first 2500 points of the transducer signal to recover the first 2500 points of the laser signal. Then this inverse function can be applied to the 5000 point transducer signal of Figure 6.1(c). The result is depicted in Figure 6.1(d). Here, the reflection of the laser signal is accurately recovered. This leads to the conclusion that one major problem of predicting reflected portions of the signal by applying the inverse function is inconsistent distortion or change of shape of the reflections.

6.2.2 Effects of Dispersion

This section studies the effects of dispersive behavior on the inverse function (in the frequency domain) approach. As observed in Section 6.2.1, the reflections in the measured data are of complex shape. Since the measured dispersion curves (Lamb waves) contain a relatively large amount of mode-information (many modes and thus overlapping regions), the dispersion will be synthetically generated so that its effects can be understood using simpler signals. Note that other researchers (Wilcox [31]) first compensate for the dispersion and then apply methods for further analysis of the dispersion compensated signals. However, this approach allows only compensation for the dispersion of one single mode and is therefore not suitable for this research.

Consider Figure 6.2(a), where the windowed first arrival of the laser source Rayleigh signal (Figure 6.1(b)) is modified in the following manner: Two filters are applied to this original signal — one Butterworth band-stop filter (band-stop from 1.5 MHz thru 4 MHz and filter-order of 4) and one Butterworth band-pass filter (band-pass from 1.5 MHz thru 4 MHz). This filtering procedure returns two separate time signals, one which contains only the frequencies between 1.5 MHz and 4 MHz, and one with the remaining frequency content of the original Rayleigh wave (reference wave). Now, the portion with the frequencies between 1.5 MHz and 4 MHz is taken and copied to be shifted in time. This is done to simulate two modes which both travel with an individual velocity as a function of frequency. To model the different velocities, the first signal (with the frequencies between 1.5 MHz and 4 MHz) is delayed by 2 μsec (slow mode) relative to the base wave and its copy is modified to arrive 2 μsec earlier (fast mode) than the base wave. Finally, the three signals (reference wave, slow mode, fast mode) are added up to simulate the first dispersive arrival (between 10 - and 20 μsec in Figure 6.2(a)). For the modeled reflection (between 30 - and 50 μsec in Figure 6.2(a)), the slow mode is 0.5 μsec closer to the reference wave, whereas the fast mode propagated 1 μsec further away from the reference wave. After adding the three reflected waveforms up, the resulting signal is divided by two to model the loss of energy over a certain propagation distance. Note that the compositions of the original and the reflected waveform have both a length of 2500 points. Last but not least, the two composed waveforms are put together by appending the reflection to the original arrival, so that the entire signal has a total length of 5000 points. Since three modes with different velocities are realized, the basic features of dispersive behavior are captured in this synthesized signal.

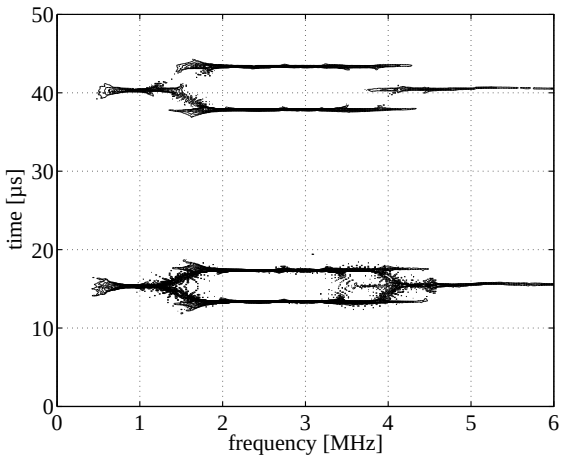

(a) Original dispersive laser signal.

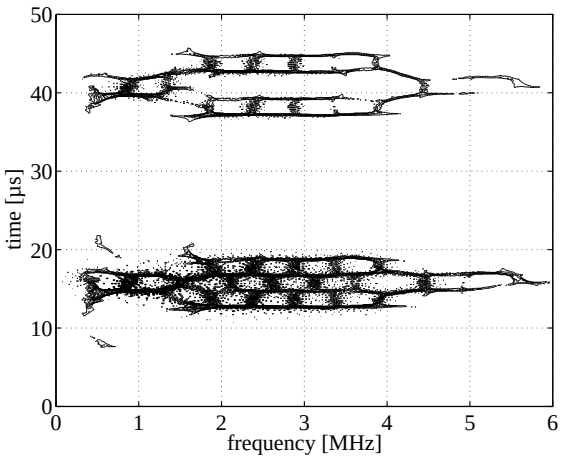

(b) Original dispersive transducer signal.

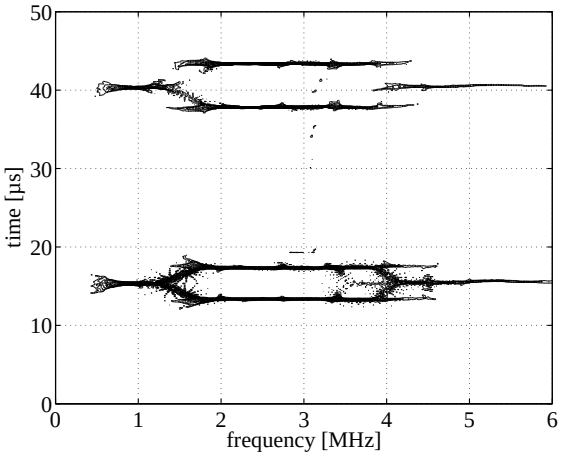

(c) Recovered dispersive laser signal.

Figure 6.2: Synthetic Dispersion.

In the second step, the exact same modifications are performed for the transducer source Rayleigh signal, in the range from 10 - thru 20 μsec as depicted in Figure 6.1(c). Now, basically the same black-box procedure as described in Section 6.2.1 is performed to calculate an inverse function for the extraction of a laser-like reflection by just providing the 5000 points long transducer signal. Therefore, first a 16384 point long inverse function is calculated in the following way:

$$S(k) = \frac{X_{\mathrm{LSR}}^{2500}(k) X_{\mathrm{TR}}^{*2500}(k)}{|X_{\mathrm{TR}}^{2500}(k)|^2 + (max|X_{\mathrm{TR}}^{2500}(k)|^2 SNR)^2} \tag{6.3}$$

where the superscript of 2500 in $X_{\mathrm{LSR}}^{2500}(k)$ and $X_{\mathrm{TR}}^{2500}(k)$ denotes that the length of the signals for calculating the inverse function is 2500 points (25 μsec) in the time

domain. For this calculation a very low noise level of 0.05 % is assumed — this choice can be justified by considering that the first arrival and the reflection are essentially the same and therefore no additional superimposed noise has to be considered. To observe how the obtained inverse function recovers the laser signal — especially the reflection between 30 - and 50 μsec — look at Figure 6.2(c). The recovery is performed as written in Equation (6.4).

$$\hat{X}_{\mathrm{LSR}}^{5000}(k) = S(k) X_{\mathrm{TR}}^{5000}(k) \tag{6.4}$$

where $\hat{X}_{\mathrm{LSR}}^{5000}(k)$ denotes the recovered 5000 points long (50 μsec) laser source signal and $X_{\mathrm{TR}}^{5000}(k)$ the original 5000 points long transducer source signal. As depicted, the reflection in the laser source signal is accurately recovered. Thus, it is confirmed that the inverse function approach is applicable for dispersive multi-mode signals.

CHAPTER 7

Conclusions and Future Work

7.1 Summary and Conclusions

This research provides background information and a detailed discussion of results for the application of signal processing methods to experimentally measured ultrasonic guided wave data from both, dispersive and non-dispersive media. Six experimentally measured data sets are acquired with a source receiver distance of 46 mm. Three of the measurements are performed on a plate to obtain dispersive Lamb waves and the three other measurement sets are performed on a half space to obtain non-dispersive Rayleigh waves. The three measurement sets are further divided into one set made with 101 laser source measurements (with equal step of 0.1 mm separating each measurement location equally distributed around 46 mm propagation distance), one set made with a piezo disc source, and one set made with a commercial transducer source. All the waveforms are detected with a laser interferometer (in normal direction to the specimen surface). The objective is to calculate a source time function and spatial weights which describe and capture the effects of the piezo disc or the transducer. During this research, the Toeplitz recursion algorithm was modified and optimized to yield improved results for the relatively long length of the acquired data sets. This was done by applying exponential windows to the data sets in order to have a smooth transition between zero and non-zero values and thus obtain a perfect reconstruction of the signals. Note that the Toeplitz recursion calculates the source function in the time domain.

Furthermore, a second method that calculates the source function in the frequency domain (also in the presence of noise) is provided. Both methods are compared for

different noise levels. The outcome of this comparison is that the time domain procedure shows amplitude and phase distortion for noisy signals, whereas the frequency domain method only changes the amplitude. The frequency domain decovolution is also used to calculate an inverse source function without any physical interpretation in the time domain (black-box approach); only time domain deconvolution is used for physical interpretation purposes due to the restricted length of the recovered source function. Both frequency and time domain deconvolution are applied to the six measurement sets. The source functions extracted by using only a single laser source signal are difficult to interpret, especially the ones obtained from the Lamb wave measurements. However the key features of diploe-like behavior and spatial extent of the piezo disc and the transducer are observed. It is also shown that the source functions from the half space and plate measurements are not the same due to reverberations in the plate that are affected and modified boundary conditions, i.e., the thickness of the inspected specimen relative to the source diameter plays a major role for the shape of the extracted source time function.

Inspections of the dispersion relationship obtained from the piezo disc and transducer are performed. It is found that temporal effects do not distort the dispersion curves but act as a bandpass filter. The spatial extent of the piezo disc or transducer is modeled by a weighted average of the laser source measurements. Different spatial weight distributions of the single laser source signals are tested and compared with the piezo disc and transducer (dispersion relationship in the spectrograms), and it is shown that a Gaussian weight distribution best models an oil-coupled transducer, whereas an inverted Gaussian weight distribution best models a glued piezo disc. Note that the methodologies presented here are also applicable to any other mechanical source with a finite spatial extent that is in contact with the specimen. An algorithm — called double iterative least squares optimization — is implemented to perform source inversion and calculation of the optimal (in least squares sense) weight distribution of the single laser signals simultaneously. The outcome of this algorithm confirms the general nature of the weight distributions obtained by the forward modeling approach as being Gaussian-like for the transducer and inverted Gaussian-like for the piezo disc.

A general approach for evaluating models by inspecting the source function in the time domain is outlined; this approach is suitable for the evaluation and comparison of models. It not only allows one to draw "right-wrong" conclusions, but also has potential for interpreting model mismatches and their seriousness.

The "black-box" approach in the frequency domain is originally performed on Lamb wave signals to recover a laser-like reflection by applying an inverse function to a measured transducer source signal. This inverse function is calculated (in the frequency domain) to recover the first arrival of a laser source signal out of the first arrival of a transducer source signal. It was not possible to recover the subsequent reflection of the laser signal from the entire transducer signal. However, using synthetic examples, it is shown that this approach works well for Rayleigh signals as well as for dispersive signals (Lamb waves). Hence, the measured reflections are observed and it is found that the shape of the reflections differ from the shape of the waveform of the original arrival.

7.2 Future Work

As mentioned in Chapter 3, only out-of-plane measurements were performed. However, the piezo disc and transducer also excite an in-plane-component which could be measured. To further improve the model of the piezo disc and the transducer, this in-plane component can be measured and considered in the forward modeling approach.

For another future consideration, a piezo disc or transducer should also be used as a receiver and a receiver function $r(n)$ can be calculated. This would give the ability to use a laser source and a laser receiver for a baseline measurement and then for later considerations a piezo discs or a transducers could be used as source and receiver. By removing the effect of the source and the receiver functions from the measured waveforms (made with piezo disc or transducer only), ideally a waveform should be obtained similar to one made with laser source and laser receiver.

AppendixA

Reflection Recovery of Measured Data

This sections shows the recovery of a reflection of actually measured transducer source Rayleigh data. The recovery is performed as outlined in Section 5.2. The inverse function is calculated with Equation (A.1).

$$S(k) = \frac{X_{\mathrm{LSR}}^{2500}(k) X_{\mathrm{TR}}^{*2500}(k)}{|X_{\mathrm{TR}}^{2500}(k)|^2 + (max|X_{\mathrm{TR}}^{2500}(k)|^2 SNR)^2} \tag{A.1}$$

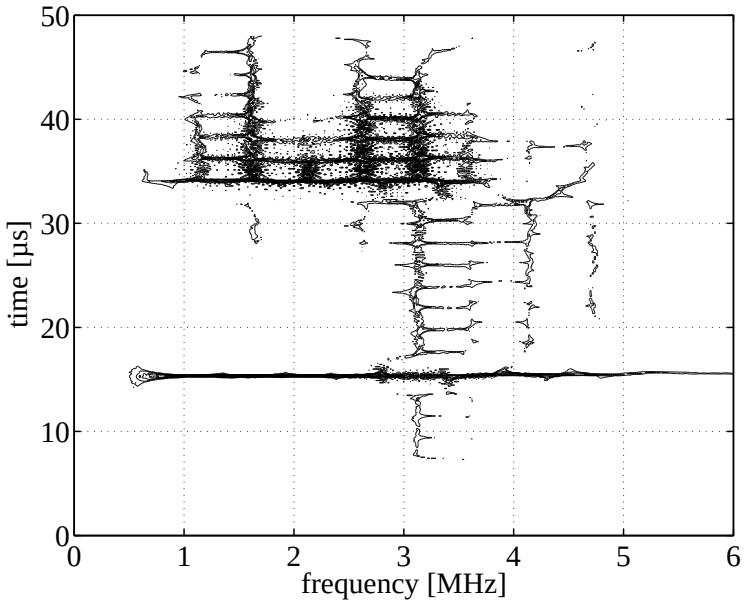

Figure A.1: Recovery of the reflection for the actually measured Rayleigh data.

Then the inverse function $S(t)$ is applied as shown in Equation (A.2).

$$\hat{X}_{\mathrm{LSR}}^{5000}(k) = S(k) X_{\mathrm{TR}}^{5000}(k) \tag{A.2}$$

$\hat{X}_{\mathrm{LSR}}^{5000}(k)$ denotes the recovered laser source Rayleigh signal depicted in Figure A.1 for the measured transducer source Rayleigh signal (5000 points). It is shown that the region of interest (at 34 μsec) is recovered poorly (it does not have the characteristics of the laser Rayleigh wave). However, the arrival time of the reflection is modeled fairly well, i.e., is consistent with the measured laser source Rayleigh data in Figure 6.1(a). Note the distortion of the reflection in the time range between 34 μsec to 48 μsec (Figure A.1).

Bibliography

[1] J. D. Achenbach. *Wave propagation in elastic solids*. North-Holland, 1975.

[2] F. Auger and P. Flandrin. Improving the readability of time-frequency and time-scale representations by the reassignment method. *IEEE transactions on signal processing*, 43:1068–1089, 1995.

[3] R. Benz. Localization of notches with Lamb waves. Master's thesis, Georgia Institute of Technology, aug 2002.

[4] R. Benz, M. Niethammer, S. Hurlebaus, and L. J. Jacobs. Localization of notches with Lamb waves. *Journal of the Acoustical Society of America*, 114:677–685, 2003.

[5] D. A. Bruttomesso, L. J. Jacobs, and R. D. Costley. Development of interferometer for acoustic emission testing. *Journal of Engineering Mechanics*, 199:2303–2316, 1993.

[6] C. Chang. Source characterization of point-like and distributed sources of acoustic emission. Dissertation Cornell University, 1985.

[7] D. E. Chimenti. Guided waves in plates and their use in materials characterization. *Applied Mechanics Review*, 50:247–284, 1997.

[8] J. Ching, A. C. To, and S. D. Glaser. Microseismic source deconvolution: Wiener filter versus minimax, Fourier versus wavelets, and linear versus nonlinear. *Journal of the Acoustical Society of America*, 115:3048–3058, 2004.

[9] L. Cohen. *Time-frequency analysis*. Prentice Hall, 1995.

[10] G. R. Cooper and C. D. McGillem. *Probablistic methods of signal and systems analysis*. Holt,Rinehart and Winston, San Francisco, 1972.

[11] L. Duquenne, E. Moulin, J. Assaad, and S. Grondel. Transient modeling of Lamb waves generated in viscoelastic materials by surface bonded piezoelectric transducers. *Journal of the Acoustical Society of America*, pages 133–141, 2004.

[12] C. Eisenhardt. Detection of cracks in plates using guided waves. Studienarbeit Universität Stuttgart, Georgia Institute of Technology, aug 1999.

[13] K. F. Graff. *Wave motion in elastic solids*. Dover publications, 1975.

[14] S. Hurlebaus. Laser generation and detection techniques for developing transfer functions to characterize the effect of geometry on elastic wave propagation. Master's thesis, Georgia Institute of Technology, sep 1997.

[15] S. Hurlebaus. A contribution to structural health monitoring using elastic waves. Dissertation Universität Stuttgart, 2002.

[16] G. Longo and B. Picinbono. *Time and frequency representations of signals and systems*. Springer Verlag, 1989.

[17] S. Mallat. *A wavelet tour*. Academic Press, 1999.

[18] J. E. Michaels. Fundamentals of deconvolution with applications to ultrasonic and acoustic emission. Master's thesis, Cornell University, may 1982.

[19] J. E. Michaels and Y.-H. Pao. The inverse source problem for an oblique force on an elastic plate. *Journal of the Acoustical Society of America*, 77:2005–2011, 1985.

[20] J. E. Michaels and Y.-H. Pao. Determination of dynamic forces from wave motion measurements. *Journal of Applied Mechanics*, 53:61–68, 1986.

[21] J. E. Michaels, T. E. Michaels, and W. Sachse. Applications of deconvolution to acoustic emmission signal analysis. *Materials Evaluation*, 39:1032–1036, 1981.

[22] M. Niethammer, L. J. Jacobs, J. Qu, and J. Jarzynski. Time-frequency representations of Lamb waves. *Journal of the Acoustical Society of America*, 109:1841–1847, 2001.

[23] A. V. Oppenheim and R. W. Schafer. *Discrete-time signal processing*. Prentice Hall, 1999.

[24] B. N. Pavlakovic, M. J. S. Lowe, D. N. Alleyne, and P. Cawley. *Disperse: A general purpose program for creating dispersion curves*. Plenum, New York, 1997.

[25] C. L. Pekeris. The seismic surface pulse. *Proceedings of the National Academy of Science of the U.S.A.*, 41:469–480, 1955.

[26] P. Pinto, S. Hurlebaus, L. Gaul, and L. J. Jacobs. Localization and sizing of discontinuities using Lamb waves. *Sturctural Health Monitoring*, pages 379–386, 2003.

[27] W. H. Prosser, D. Seale, and B. T. Smith. Time-frequency analysis of the dispersion of Lamb modes. *Journal of the Acoustical Society of America*, 105:2669–2676, 1999.

[28] E. A. Robinson. *Multichannel time series analysis with digital computer programs*. Holden-Day, San Francisco, 1967.

[29] E. A. Robinson and S. Treitel. *Geophysical signal analysis*. Prentice Hall, 1980.

[30] R. L. Weaver and Y.-H. Pao. Spectra of transient waves in elastic plates. *Journal of the Acoustical Society of America*, 72:1933–1941, 1982.

[31] P. D. Wilcox. A rapid signal processing technique to remove the effect of dispersion from guided wave signals. *IEEE Transactions on Ultrasonics, Ferroelectrics, and Frequency Control*, 50:419–432, 2003.